National Transportation Safety Board

Office of Marine Safety
Washington, D.C. 20594-2000
December 13, 2016

ATTACHMENT 13 to the METEOROLOGY GROUP FACTUAL REPORT
DCA16MM001

Study on the potential for a "rogue wave" event for the time surrounding the *El Faro* sinking provided by the College of Engineering at the Georgia Institute of Technology and the Italian Ship Model Basin.

Submitted by: Mike Richards
NTSB, AS-30

Technical Report

On the prediction of rogue waves during Hurricane Joaquin

Document Date	18 Oct 2016	
	—-	
Authors	Francesco Fedele	
	Claudio Lugni, Fabio Fucile, Emilio F. Campana	
	—-	

Georgia Tech School of Civil and Environmental Engineering
College of Engineering

The Italian Ship Model Basin
INSEAN

On the prediction of rogue waves during Hurricane Joaquin

by F. Fedele, C. Lugni, F. Fucile, E.F. Campana

The concept and design was provided by F. Fedele, who coordinated the scientific effort together with C. Lugni. C. Lugni and F. Fucile performed numerical simulations and developed specific codes for the analysis. The wave statistical analysis was performed by F. Fedele together with C. Lugni. The overall supervision was provided by F. Fedele; E. F. Campana made ongoing incisive intellectual contributions. All authors participated in the analysis and interpretation of results and the writing of the report.

Contents

1 Introduction **4**

2 Metaocean parameters of Hurricane Joaquin in the region of the sinking of El Faro **5**

3 Statistical properties of Hurricane Joaquin-generated seas **6**

4 Higher Order Spectral (HOS) simulations of the El Faro sea state **9**

5 Encounter probability of a rogue wave by a fixed observer: the return period of a wave whose crest height exceeds a given threshold **11**

6 Time profile of the simulated rogue waves **13**

7 Space-time statistics of the encountered sea state by El Faro before sinking **14**
7.1 A new stochastic space-time (FST) model 16
7.2 The encounter probability of a rogue wave by the El Faro vessel 18

8 Breaking onset of the simulated rogue waves **20**

9 Conclusions **23**

10 Recommendations **23**

Appendices **24**

Appendix A Methods **24**
A.1 Wave parameters 24
A.2 Space-Time Statistical Parameters 25
A.3 The Higher Order Spectral (HOS) numerical method 26

Summary

This report is a study on the prediction of rogue waves during Hurricane Joaquin provided as a supplement to the National Transportation Safety Board (NTSB) to assist them in their investigation of the sinking of the Merchant Vessel El Faro, which occurred east of the Bahamas on October 1, 2015. This study involved using high resolution hindcasts of hurricane-generated sea states and wave simulations combined with probabilistic models to quantify the ocean rogue wave conditions around the time and location of the accident.

Rogue waves have been observed in oceans around the world over the course of a decade. Such waves stem from a combination of constructive interference and nonlinear effects specific to the complex dynamics of ocean waves. In rare conditions, waves arrive in an organized way or almost in phase, leading to an unusual case of constructive interference that can yield resulting waves with large amplitudes. But this still cannot explain the size of real world ocean rogue waves. That difference can be accounted for by the nonlinear nature of ocean waves, which are not sinusoidal - but instead have rounded troughs, along with sharp peaks that result from the water being pushed upward against the pull of gravity. Thus, one needs to account for the nonlinearity of the ocean, which is manifested in the lack of symmetry between the crests and the troughs. These nonlinearities add onto the effects of constructive interference and yield an enhancement of the crest height, i.e. the vertical distance from the mean sea level to the top of the wave. As a result, the formation of a rogue wave at a given point of the ocean is simply chance.

Our rogue wave analysis focused on the study of the 1-hour sea state of Hurricane Joaquin during which the El Faro vessel sank. We estimated that a fixed observer at a point of the ocean has a very small probability $P_e \approx 10^{-6}$ to encounter a rogue wave whose crest height exceeds 14 meters $\approx 1.6H_s$, H_s being the significant wave height defined as four times the standard deviation of surface wave elevations. Further, this probability estimate is of the same order as those for the Andrea and Draupner rogue waves, observed at different oil platforms in the North Sea in 1995 and 2007, respectively and the Killard rogue wave observed off the coast of Ireland in 2015.

However, the data suggests that the El Faro vessel was drifting at an average speed of approximately 2.5 m/s prior to its sinking. As a result, El Faro has a higher probability to encounter a rogue wave while drifting over a period of time. Indeed, the encounter of a rogue wave by a moving vessel is analogous to that of a big wave that a surfer is in search of. The surfer's likelihood to encounter a big wave increases if he moves around a large area instead of staying still; if he spans a large area the chances to encounter a large wave increase. This is a space-time effect very important for ship navigation and it cannot be neglected. Such an effect is considered in our rogue wave analysis by way of a new probabilistic model for the prediction of rogue waves encountered by a vessel along its navigation path. In particular, we give a theoretical formulation and interpretation of the encounter probability of a rogue wave by a moving vessel. This probability is unconditional as it is not conditioned on the event that the sinking of El Faro happened.

According to our analysis, the probability that El Faro encounters a rogue wave whose crest height exceeds 14 meters while drifting over a time interval of 10 minutes is $P_e \approx 1/400$. We also observed that the encounter probability does not scale linearly with time because of

nonlinearities that reduce the natural dispersion of waves. Indeed, assuming that the vessel drifts over a time interval 5 times longer (50 minutes), the encounter probability is roughly 3 times larger, i.e. $P_e \approx 1/130$.

The predicted rogue wave has similar generating mechanism and characteristics of the Andrea, Draupner and Killard rogue waves. We found that the main mechanism responsible for generating these waves is the constructive interference of elementary waves enhanced by bound nonlinearities and space-time effects, in agreement with recent studies by the first author. An analysis of the kinematics of the simulated rogue waves suggests that such waves were nearly incipient breaking, limiting the likelihood of larger rogue events.

The present analysis provides the basis for an improved understanding of how rogue waves originate during hurricanes and could lead to improved techniques for identifying ocean areas likely to spawn them, allowing shipping companies to avoid dangerous seas.

1 Introduction

The tragic sinking of the SS El Faro vessel occurred while it was traveling from Florida to Puerto Rico. The vessel with a crew of 33 sank about 1140 Hrs UTC on Oct. 1, 2015.

As part of their investigation into the sinking of the El Faro, the National Transportation Safety Board (NTSB) has requested an analysis on the occurrence of rogue waves during Hurricane Joaquin around the time and location of the El Faro's sinking. To do so, we used as an input the WAVEWATCH III[1] hindcast sea states provided by the National Oceanic and Atmospheric Administration (NOAA) for the time period and region that correspond to the sinking of the El Faro vessel.

The report is structured as follows. In section 2, we will discuss the sea states characteristics and wave extremes of the Hurricane Joaquin as it passed through the region of the sinking of El Faro. The convenient wave parameters and statistical models are defined in Appendix A.1. We use the directional spectra of the hindcast hourly sea states, which describe the complex energy flow of the associated wave field as an output of WAVEWATCH III.

In section 3, we discuss the statistical properties of the sea states generated by Hurricane Joaquin. Then, in section 4 we focus on the study of the 1-hour sea state during which the El Faro vessel sank, hereafter referred to El Faro sea state. We exploit a higher order spectral method to solve numerically for the Euler equations governing the dynamics of the ocean wave field. Initial conditions for the wave field are obtained from the directional spectrum as an output of WAVEWATCH III. In sections 5 and 6, we present the rogue wave analysis for the El Faro sea state. In particular, we first study the encounter probability of rogue waves by a fixed observer at a given point of the ocean. The largest simulated rogue wave and its generating mechanism and characteristics are then compared to those of the Andrea and Draupner rogue waves, observed at different oil platforms in the North Sea in 1995 and 2007, respectively, and the Killard rogue wave observed off the coast of Ireland in 2015.[2] The metaocean parameters of the four sea states are summarized in Table 1.

In section 7 we study the space-time statistical properties of the El Faro sea state by way of a new probabilistic model for the prediction of rogue waves encountered by a vessel along its navigation path. In particular, we give a theoretical formulation of the encounter probability of a rogue wave by a moving vessel and its statistical interpretation. The data suggest that the El Faro vessel was drifting at an estimated average speed of approximately 2.5 m/s prior to its sinking. Thus, we estimate what is the unconditional probability that El Faro encounters a rogue wave while drifting over a given period of time.

Then, in Section 8 we present results on the breaking onset of the simulated rogue waves. Conclusions in Section 9 and specific recommendations for future analyses and studies in Section 10 are finally provided.

	El Faro	**Andrea**	**Draupner**	**Killard**
Significant wave height H_s [m]	9.0	10.0	11.2	11.4
Dominant wave period T_p [s]	10.2	14.3	15.0	17.2
Mean zero-crossing wave period T_0 [s]	9.2	11.1	11.3	13.2
Mean wavelength L_0 [m]	131	190	195	246
Depth d [m], $k_0 d$	4700, 263	74, 2.23	70, 2.01	58, 1.36
Spectral bandwidth ν	0.49	0.35	0.36	0.37
Angular spreading σ_θ	0.79	0.43	0.44	0.39
Parameter $R = \sigma_\theta^2/2\nu^2$ [3]	1.34	0.72	0.75	0.56
Benjamin Feir Index BFI in deep water [4]	0.36	0.24	0.23	0.18
Tayfun NB skewness $\lambda_{3,NB}$ [5]	0.26	0.159	0.165	0.145
Mean skewness λ_3 from HOS simulations	0.162	0.141	0.146	0.142
Maximum NB dynamic excess kurtosis $\lambda^d_{40,max}$ [6]	10^{-3}	$1.3 \cdot 10^{-3}$	$1.1 \cdot 10^{-3}$	$1.6 \cdot 10^{-3}$
Janssen NB bound excess kurtosis $\lambda^d_{40,NB}$ [7]	0.049	0.065	0.074	0.076
Mean excess kurtosis λ_{40} from HOS simulations	0.042	0.041	0.032	-0.011
Actual maximum crest height h/H_s	1. 68	1.55	1.63	1.62
Actual maximum crest-to-trough (wave) height H/H_s	2.6	2.30	2.15	2.25

Table 1: Wave parameters and various statistics of the simulated El Faro sea state in comparison to the Andrea, Draupner and Killard rogue sea states.[2] We refer to Appendix A.1 for the definitions of the wave parameters.

2 Metaocean parameters of Hurricane Joaquin in the region of the sinking of El Faro

In this section, we use the hindcast directional spectra by WAVEWATCH III and describe the wave characteristics of the sea states generated by Hurricane Joaquin about the time and location where the El Faro vessel sank. In the following we refer to Appendix A.1 for the definitions of metaocean parameters and details.

The top panel on the left of Fig. (1) shows hourly variations of the significant wave height H_s during the event. The top-right panel displays the history of the dominant wave period T_p, and the dominant wave direction, the U_{10} wind speed and direction are shown in the bottom-panels respectively. The red vertical lines delimit the 1–hour interval during which the El Faro vessel sank. The hourly variations of the mean wavelength L_0 and associated mean wave period T_0 are shown in Fig. (2).

The encountered 1-hour sea state by El Faro about the time and location of sinking, hereafter referred to as El Faro sea state, had a significant wave height of $H_s \approx 9$ m and it was very multidirectional (short-crested) as indicated by the large values of both the spectral bandwidth ν and angular spreading θ_v as seen in Fig. (3).

In Table 1 we report the metaocean parameters of the El Faro sea state in comparison to those of the Draupner, Andrea and Killard rogue sea states.[2] Note that the four sea states have similar metaocean characteristics. However, El Faro is a steeper sea state as the mean wavelengh L_0 is shorter than the other three states.

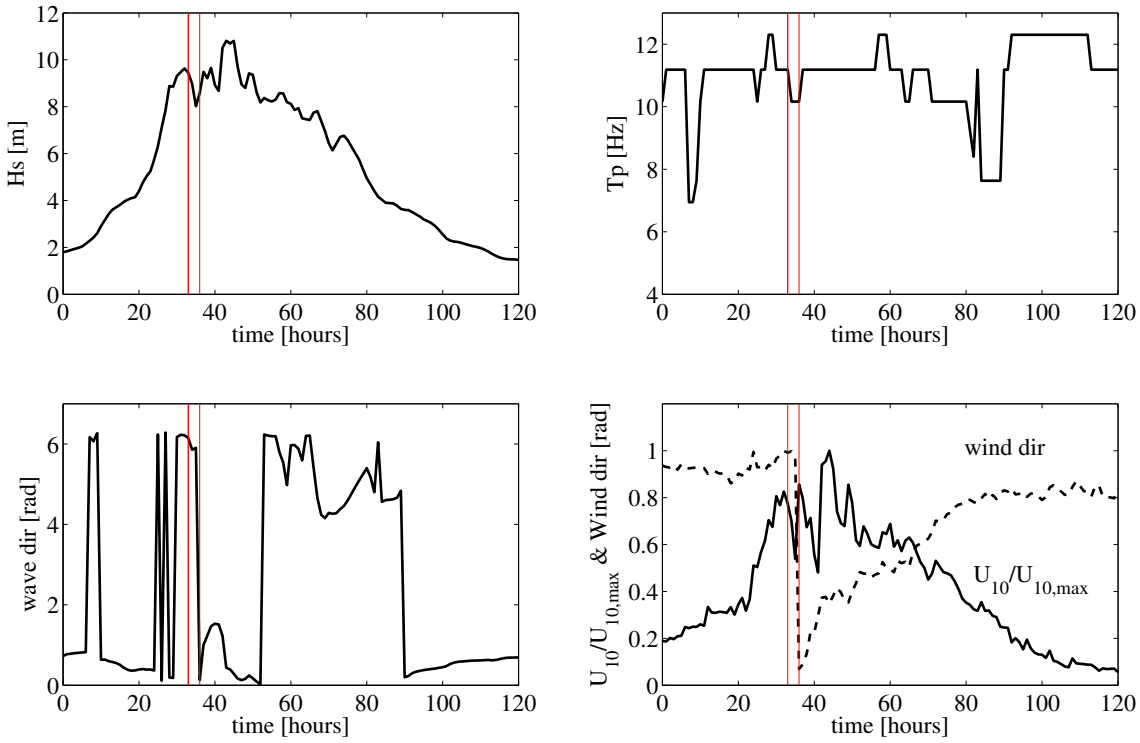

Figure 1: WAVEWATCH III parameters history during Hurricane Joaquin around the location where the El Faro vessel sank. (top-left) Hourly variation of the significant wave height H_s, (top-right) dominant wave period T_p, (bottom-left) dominant wave direction and (bottom-right) normalized $U_{10}/U_{10,max}$ wind speed (solid line) and direction (dashed line). Maximum wind speed $U_{10,max} \approx 51$ m/s. Red vertical lines delimit the 1–hour interval during which the El Faro vessel sank.

3 Statistical properties of Hurricane Joaquin-generated seas

The relative importance of ocean nonlinearities can be measured by integral statistics such as the wave skewness λ_3 and the excess kurtosis λ_{40} of the zero-mean surface elevation $\eta(t)$:

$$\lambda_3 = \overline{\eta^3}/\sigma^3, \qquad \lambda_{40} = \overline{\eta^4}/\sigma^4 - 3\,. \tag{1}$$

Here, overbars imply statistical averages and σ is the standard deviation of surface wave elevations (see Appendix A.1 for definitions of the statistical parameters and details). For second-order waves in deep water[8]

$$\lambda_3 \approx 3\mu_m(1 - \nu + \nu^2), \tag{2}$$

and the following bounds hold[5]

$$3\mu_m(1 - \sqrt{2}\nu + \nu^2) \leq \lambda_3 \leq 3\mu_m. \tag{3}$$

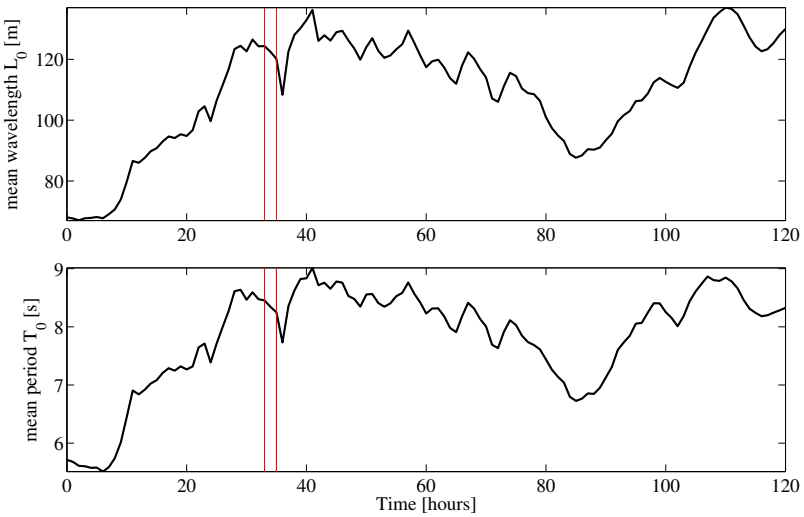

Figure 2: WAVEWATCH III parameters history during Hurricane Joaquin around the location where the El Faro vessel sank. (top) Hourly variation of the mean wavelength L_0 history and (bottom) associated mean wave period T_0. Red vertical lines delimit the 1-hour interval during which the El Faro vessel sank.

Here, ν is the spectral bandwidth and the characteristic wave steepness $\mu_m = k_m\sigma$, where k_m is the wavenumber corresponding to the mean spectral frequency ω_m.[9] For narrowband (NB) waves, ν tends to zero and the associated skewness $\lambda_{3,NB} = 3\mu_m$.[8–10]

The skewness coefficient represents the principal parameter with which we describe the effects of second-order bound nonlinearities on the geometry and statistics of the sea surface with higher sharper crests and shallower more rounded troughs.[8–10] The excess kurtosis comprises a dynamic component due to third-order quasi-resonant wave-wave interactions and a bound contribution induced by both second- and third-order bound nonlinearities.[3,8–12]

For third-order nonlinear random seas the excess kurtosis

$$\lambda_{40} = \lambda_{40}^d + \lambda_{40}^b \tag{4}$$

comprises a dynamic component λ_{40}^d due to nonlinear quasi-resonant wave-wave interactions[3,4] and a Stokes bound harmonic contribution λ_{40}^b.[7] Janssen[7] derived a complex general formula for the bound excess kurtosis. For narrowband (NB) waves, the formula is more compact (see Eq. (A23) in[7] and Appendix A.1). For instance, in deep water it reduces to the simple form $\lambda_{40,NB}^b = 18\mu_m^2 = 2\lambda_{3,NB}^2$[3,7,13] where $\lambda_{3,NB}$ is the skewness of narrowband waves.[9]

As for the dynamic component, Fedele[6] recently revisited Janssen's[4] weakly nonlinear formulation for λ_{40}^d. In deep water, this is given in terms of a six-fold integral that depends on the Benjamin-Feir index $BFI = \mu_m/\sqrt{2}\nu$ and the parameter $R = \sigma_\theta^2/2\nu^2$, which is a dimensionless measure of the multidirectionality of dominant waves.[3,14] Here, ν is the spectral bandwidth and σ_θ denotes angular spreading.[3,14] As waves become unidirectional (1D) waves R tends to zero.

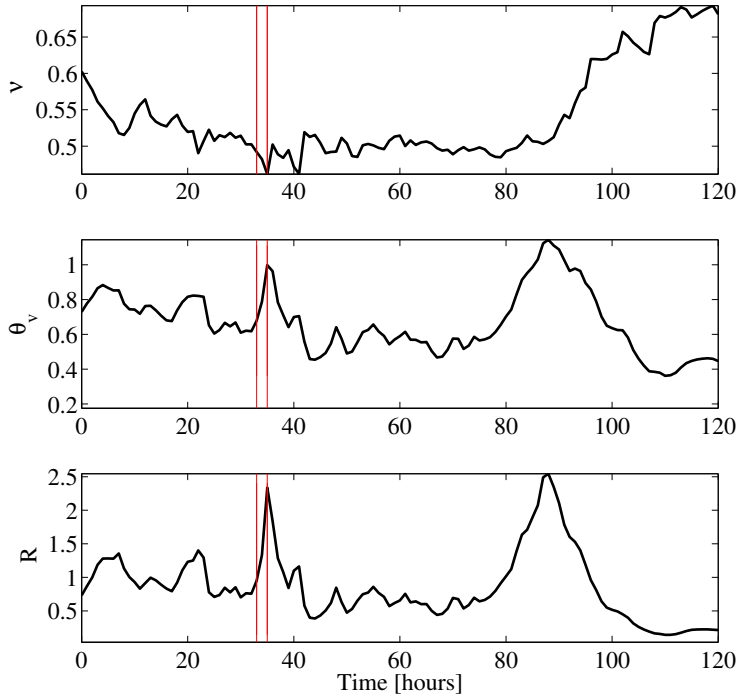

Figure 3: WAVEWATCH III parameters history during Hurricane Joaquin around the location where the El Faro vessel sank. (top) Hourly variation of the spectral bandwidth ν history, (center) directional spreading θ_v and (bottom) directional factor $R = \frac{1}{2}\nu^2/\theta_v^2$. Red vertical lines delimit the 1-hour interval during which the El Faro vessel sank.

Recent theoretical results clearly show that third-order quasi-resonant interactions play an insignificant role in the formation of large waves in realistic oceanic seas.[2,6] Further, oceanic evidence available so far[10,15,16] seems to suggest that the statistics of large oceanic wind waves are not affected in any discernible way by quasi-resonant nonlinearities, including NLS-type modulational instabilities that attenuate as the wave spectrum broadens.[17] However, bound nonlinearities affect both skewness and kurtosis as they shape the wave surface with sharper crests and shallower troughs.

The bottom panel of Fig. (3) displayes the hourly variations of the directional factor R during Hurricane Joaquin near the location where El Faro sank. About the peak of the hurricane the generated sea states are very multidirectional (short-crested) as $R > 1$ and so wave energy can spread directionally. As a result, nonlinear focusing due to modulational instability effects diminishes[6,18–20] and becomes essentially insignificant under such realistic oceanic conditions.[2,6,21,22]

The top panel of Fig. (4) displayes the hourly variation of the Tayfun steepness μ (solid line) with bounds (dashed lines). The excess kurtosis λ_{40} mostly due to bound nonlinearities is shown in the center panel and the associated Λ parameter at the bottom. The red vertical lines delimit the 1-hour interval during which the El Faro vessel sank.

In Table 1 we compare the statistical parameters of the El Faro sea state and the Draup-

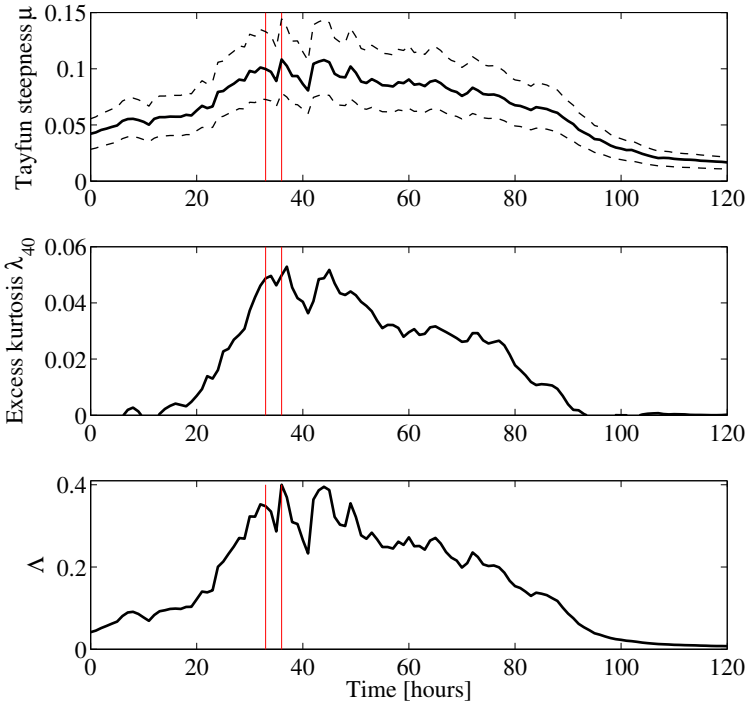

Figure 4: WAVEWATCH III parameters history during Hurricane Joaquin around the location where the El Faro vessel sank. (top) Hourly variation of the Tayfun steepness μ (solid line) with bounds (dashed lines), (center) excess kurtosis λ_{40} and (bottom) nonlinear coefficient $\Lambda \sim 8\lambda_{40}/3$. Red vertical lines delimit the 1-hour interval during which the El Faro vessel sank.

ner, Andrea and Killard rogue sea states.[2] Note that the El Faro sea state has the largest directional spreading. Moreover, for all the four sea states the respective BFI parameters are less than unity and the maximum dynamic excess kurtosis is of $O(10^{-3})$ and thus negligible in comparison to the associated bound component. Hereafter, this will be confirmed further by a quantitative analysis based on simulations of the El Faro sea state.

4 Higher Order Spectral (HOS) simulations of the El Faro sea state

We have performed numerical simulations of the El Faro sea state during which the vessel sank in order to investigate the statistical properties and rogue waves of the wave field encountered by the El Faro vessel. To attain high accuracy and efficiency in the numerical simulations we used the Higher-Order pseudo-Spectral (HOS) method[23,24] to solve for the nonlinear wave propagation problem modeled by the Euler equations. In particular, the associated initial boundary value problem for the Laplace equation with nonlinear boundary conditions on the free-surface is solved by way of a perturbation expansion of the potential

velocity field up to a prescribed order of nonlinearities. A detailed description of the Euler equations and of the HOS numerical method are given in Appendix A.3.

We used as an input for the HOS solver the hourly WAVEWATCH III hindcast directional spectrum $S(f, \theta)$ around the time and region of the El Faro sinking shown in Fig. 5. This is used to define the initial wave field conditions for the HOS simulations. The hindcast spectrum is the result of a balance among wind input, four-wave resonance nonlinearities and wave breaking. Our HOS simulations are performed accounting only for the full (resonant and bound) nonlinearities of the Euler equations up to fourth order in wave steepness.

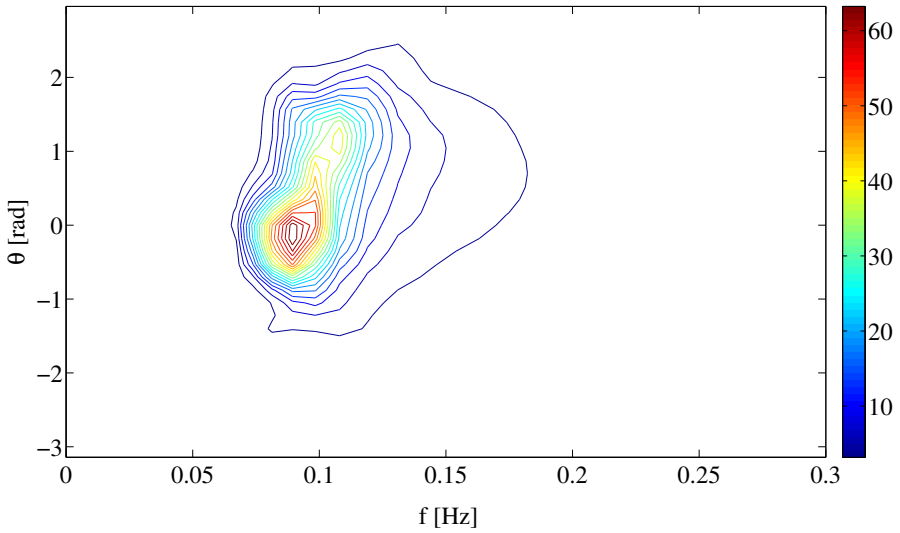

Figure 5: WAVEWATCH III hindcast directional spectrum $S(f, \theta)$ $[m^2 s/rad]$ at approximately the time and location of the El-Faro sinking.

The first set of simulations of the El Faro sea state have a duration of at least 30 minutes to a maximum of 1 hour, the computational domain D_1 has an area of 2 km x 2 km and we resolve the wave field using 512 x 512 Fourier modes. A second set of simulations have been performed for a larger computational domain D_2 of area 4 km x 4 km with doubled number of Fourier modes (1024 x 1024) to keep the same resolution.

In order to quantify the effects of nonlinearities (free and bound harmonic interactions) on the wave propagation, we have examined the wavenumber-frequency spectrum $S(k, \omega)$ estimated from the HOS simulations of the El Faro sea state over the larger domain D_2 for a duration of 30 min. This is shown in Figure 6, where dashed lines denote the theoretical dispersion curves associated with the first-order (1^{st}) free waves as well as the second (2^{nd}) and third-order (3^{rd}) bound harmonic waves. We observe that the HOS predictions indicate that second order nonlinearities are dominant with a weak effect of third-order nonlinear bound interactions, in agreement with recent studies of rogue sea states.[2]

We also observed insignificant differences between third-order and fourth-order HOS simulations. Further, the associated statistical parameters such as skewness and kurtosis rapidly reach a steady state as an indication that quasi-resonant wave-wave interactions due to modulation instabilities are negligible in agreement with theoretical predictions[6] and simulations.[2]

Note that theoretical narrowband predictions slightly overestimate the simulated values for skewness and excess kurtosis (see Table 1). The same trend is also observed in recent studies on rogue waves.[2] This is simply because narrowband approximations do not take into account the directionality and the finite bandwidth of the wave spectrum of the El Faro sea state.

Hereafter, we will investigate the wave statistics and rogue waves of the simulated El Faro sea state.

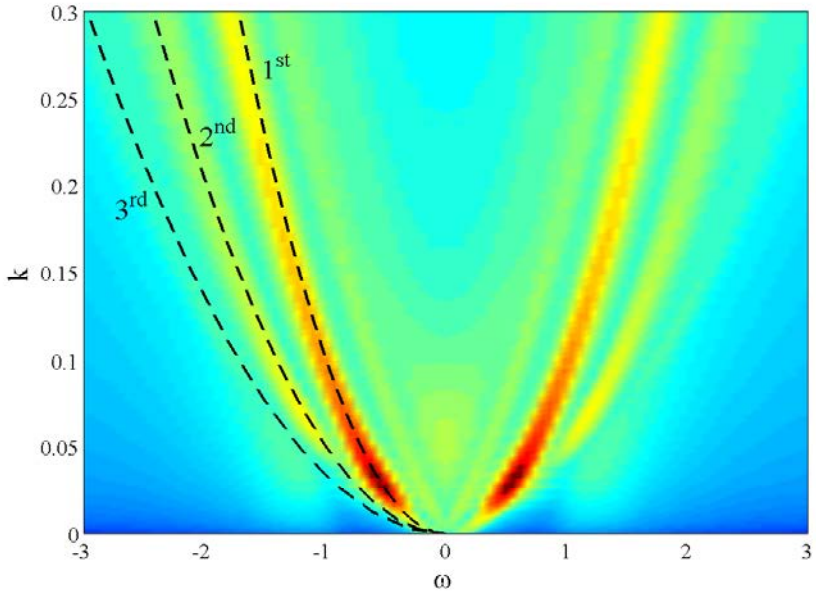

Figure 6: HOS simulations of the El Faro sea state: predicted wavenumber-frequency spectrum $S(k,\omega)$ $[m^2 s/rad]$. Dashed lines denote the theoretical dispersion curves associated with first-order (1^{st}) free waves as we all as second (2^{nd}) and third-order (3^{rd}) bound harmonic waves.

5 Encounter probability of a rogue wave by a fixed observer: the return period of a wave whose crest height exceeds a given threshold

To describe the statistics of rogue waves encountered by a fixed observer at a given point of the ocean, we consider the conditional return period $N_h(\xi)$ of a wave whose crest height exceeds the threshold $h = \xi H_s$, namely

$$N_h(\xi) = \frac{1}{\Pr\{h > \xi H_s\}} = \frac{1}{P(\xi)}, \tag{5}$$

where $P(\xi)$ is the probability of a wave crest height exceeding ξH_s as encountered by a fixed observer. In other words, $P(\xi)$ is the probability that a wave observed at a fixed point of

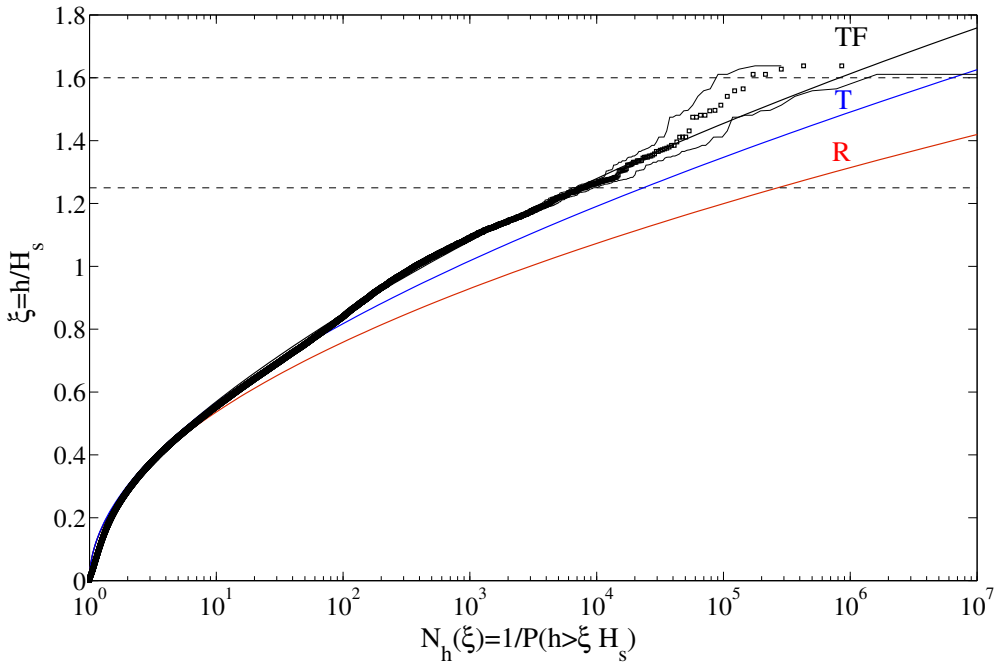

Figure 7: HOS simulations of the El Faro sea state. Crest height scaled by the significant wave height (ξ) versus conditional return period (N_h) for the (left) Andrea, (center) Draupner and (right) Killard rogue sea states: HOS numerical predictions ($\square$) in comparison with theoretical models (T=second-order Tayfun (light solid lines), TF=third-order (red solid lines) and R=Rayleigh distributions (dark dashes)). Confidence bands are also shown (light dashes). $N_h(\xi)$ is the inverse of the exceedance probability $P(\xi) = \Pr\{h > \xi H_s\}$. The two horizontal lines denote the rogue threshold $1.25H_s$[25] and $1.6H_s$ respectively.

the ocean has a crest height that exceeds the threshold ξH_s. Equation (5) also implies that the threshold ξH_s, with $H_s = 4\sigma$, is exceeded on average once every $N_h(\xi)$ waves.

For weakly nonlinear random seas, the probability P can be described by the (third-order) TF, (second-order Tayfun) T or (linear Rayleigh) R distributions. In particular,[10]

$$P_{TF}(\xi) = \Pr\{h > \xi\, H_s\} = \exp\left(-8\,\xi_0^2\right)\left[1 + \Lambda\xi_0^2\left(4\,\xi_0^2 - 1\right)\right], \tag{6}$$

where ξ_0 follows from the quadratic equation $\xi = \xi_0 + 2\mu\,\xi_0^2$.[9] Here, the Tayfun wave steepness $\mu = \lambda_3/3$ is of $O(\mu_m)$ and it is a measure of second-order bound nonlinearities as it relates to the skewness of surface elevations.[8] The parameter Λ is a measure of third-order nonlinearities as a function of the fourth order cumulants of the wave surface.[10] In our studies it is approximated by $\Lambda_{\text{appr}} = 8\lambda_{40}/3$ (see Appendix A.1). For second-order seas, hereafter referred to as Tayfun sea states,[26] $\Lambda = 0$ only and P_{TF} in Eq. (9) yields the Tayfun (T) distribution[9]

$$P_T(\xi) = \exp\left(-8\xi_0^2\right). \tag{7}$$

For Gaussian seas, $\mu = 0$ and $\Lambda = 0$ and P_{TF} reduces to the Rayleigh (R) distribution

$$P_R(\xi) = \exp\left(-8\xi^2\right). \tag{8}$$

Note that the Tayfun distribution represents an exact result for large second order wave crest heights and it depends solely on the steepness parameter defined as $\mu = \lambda_3/3$.[8]

Our statistical analysis of HOS wave data suggest that second-order effects are the dominant factors in shaping the probability structure of the El Faro sea state with a minor contribution of excess kurtosis effects. Such dominance is seen in Fig. 7, where the HOS numerical predictions of the conditional return period $N_h(\xi)$ of a crest exceeding the threshold ξH_s are compared against the theoretical predictions based on the linear Rayleigh (R), second-order Tayfun (T) and third-order (TF) models from Eq. (9). In particular, $N_h(\xi)$ follows from Eq. (5) as the inverse $1/P(\xi)$ of the empirical probabilities of a crest height exceeding the threshold ξH_s. An excellent agreement is observed between simulations and the third-order TF model, which slightly exceeds the second-order T model as an indication that second-order effects are dominant, whereas the linear Rayleigh model underestimates the empirical return periods.

For both third- and fourth-order nonlinearities, the return period N_r of a wave whose crest height exceeds the rogue threshold[25] $1.25H_s \approx 11$ m is nearly $N_r \sim 10^4$ for the El Faro sea state and for the simulated Andrea, Draupner and Killard rogue sea states.[2] This is in agreement with oceanic rogue wave measurements,[16] which indicate that the rogue threshold for crest heights is exceeded on average once every $N_r \sim 10^4$ waves. Similarly, recent measurements off the west coast of Ireland[27] yield $N_r \sim 6 \cdot 10^4$. In contrast, in a Gaussian sea the same threshold is exceeded more rarely and on average once every $\sim 3 \cdot 10^5$ waves.

Note that the largest wave crest height observed in the simulated El Faro sea state exceeds the threshold $1.6H_s \approx 14$ m (see Table 1). This is exceeded on average once every 10^6 waves in a time series extracted at a point in third- and fourth-order seas and extremely rarely in Gaussian seas, i.e. on average once every 10^9 waves. This implies that rogue waves observed at a fixed point of the ocean are likely to be rare occurrences of weakly random seas, or Tayfun sea states.[26] Our results clearly confirm that rogue wave generation is the result of the constructive interference (focusing) of elementary waves enhanced by bound nonlinearities in agreement with the theory of stochastic wave groups proposed by Fedele and Tayfun (2009),[8] which relies on Boccotti's theory of quasi-determinism.[28] Our conclusions are also in agreement with observations.[8,10,12,15]

6 Time profile of the simulated rogue waves

The wave profile η with the largest wave crest height ($> 1.6H_s \approx 14$ m, see Table 1) observed in the time series of the surface fluctuations extracted at points randomly sparse over the simulated domain of the El Faro sea state is shown in the left panel of Fig. (9) and compared against the Draupner, Andrea and Killard rogue wave profiles.[2] In the same figure, the mean sea level (MSL) below the crests is also shown. The estimation of the MSL follows by low-pass filtering the measured time series of the wave surface with frequency cutoff $f_c \sim f_p/2$, where f_p is the frequency of the spectral peak.[29]

The four wave profiles are very similar suggesting a common generation mechanism of the rogue events. Further, we observe a set-up of the MSL below the simulated El Faro rogue wave most likely due to the multidirectionality of the sea state. We point out that a set-up is also observed for the actual Draupner rogue wave. Indeed, recent studies about Draupner reported that the hindcast from the European Centre for Medium-Range Weather Forecasts shows swell waves propagating at approximately 80 degrees to the wind sea.[30] They argued that the Draupner wave may be due to the crossing of two almost orthogonal wave groups in accord with second-order theory. This would explain the set-up observed under the large wave[29] instead of the second-order set-down normally expected.[31]

Finally, the average wave profile with a crest height that exceeds the rogue threshold[25] $1.25H_s \approx 11$ m is shown in Fig. (8). The set-up of the MSL is also evident.

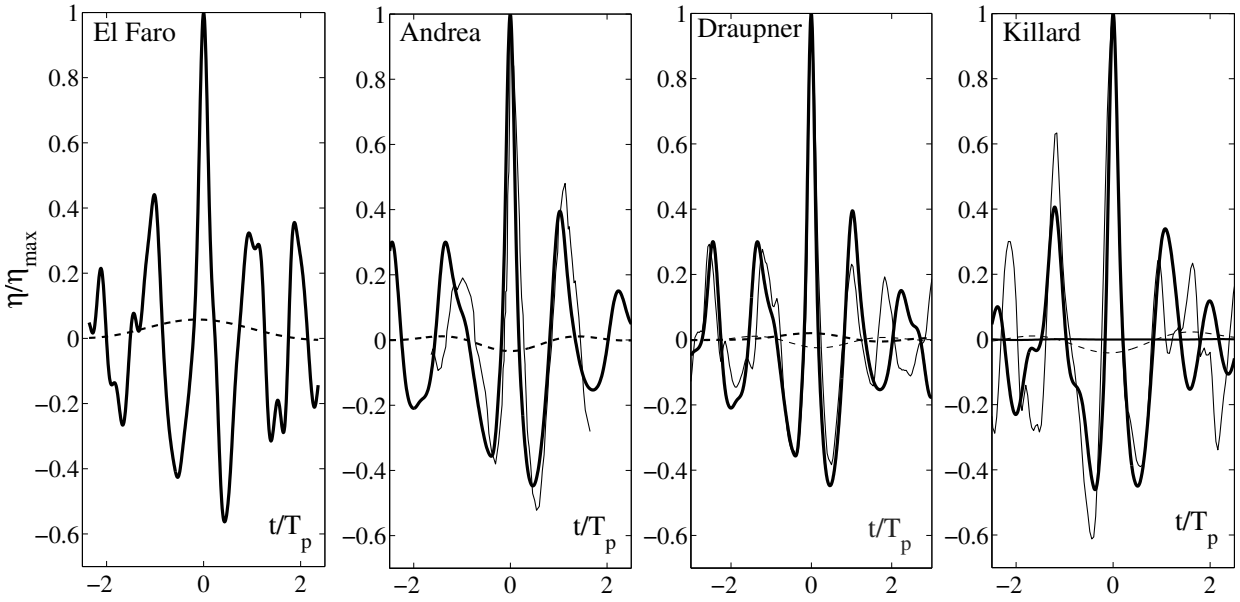

Figure 8: Third-order HOS simulated extreme wave profiles η/η_{max} (solid) and mean sea levels (MSL) (dashed) versus the dimensionless time t/T_p for (from left to right) El Faro, Andrea, Draupner and Killard waves. η_{max} is the maximum crest height given in Table 1. For comparisons, actual measurements (thick solid) and MSLs (thick solid) are also shown for Andrea, Draupner and Killard. Note that the Killard MSL is insignificant and the Andrea MSL is not available. T_p is the dominant wave period (see Appendix A.1 for definitions).

7 Space-time statistics of the encountered sea state by El Faro before sinking

The largest crest height of a wave observed in time at a given point of the ocean represents a maximum observed at that point. Clearly, the maximum wave surface height observed

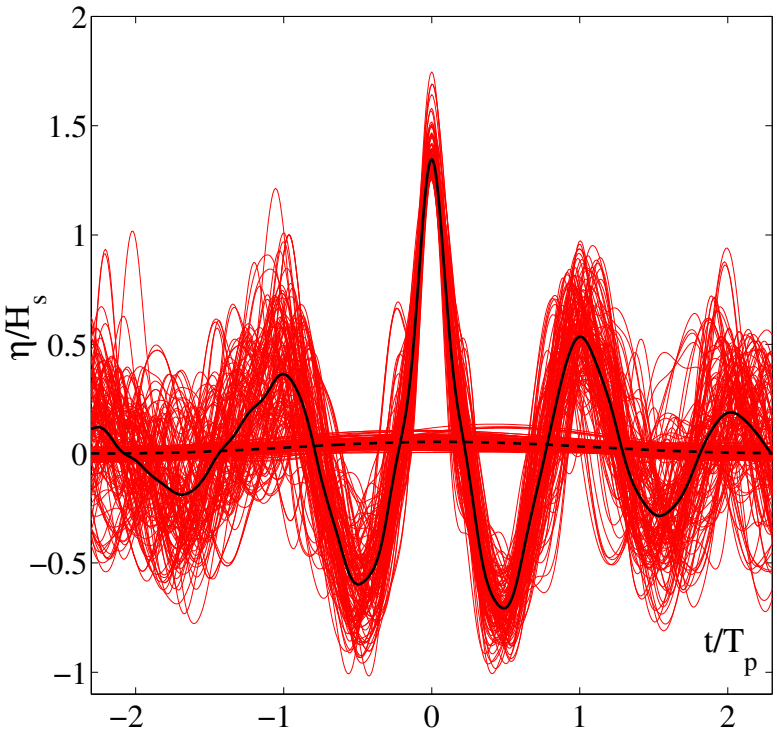

Figure 9: Third-order HOS simulated average extreme wave profile η/H_s with a crest height that exceeds the rogue threshold[25] $1.25H_s \approx 11$ m (black solid) and mean sea level (MSL) (dashed) versus the dimensionless time t/T_p, where T_p is the dominant wave period and H_s is the significant wave height (see Appendix A.1 for definitions). Red lines denote sampled time wave profiles extracted at stochastically independent random points sparse over the computational domain of the HOS simulations.

over a given area during a time interval, i.e. space-time extreme, is much larger than that observed at a given point. Indeed, in relatively short-crested directional seas such as those generated by hurricanes, it is very unlikely that an observed large crest at a given point in time actually coincides with the largest crest of a group of waves propagating in space-time. In contrast, in accord with Boccotti's quasi-determinism theory,[28] it is most likely that the sea surface was in fact much higher somewhere near the measurement point.

Space-time wave extremes can be modeled stochastically[32,33] drawing on the theory of Euler Characteristics of random fields[34–36] and nonlinear wave statistics.[10] In the following, we present a new stochastic model for the prediction of space-time extremes[32,37] that accounts for both second and third-order nonlinearities.[10,12]

7.1 A new stochastic space-time (FST) model

Drawing on Fedele's work,[32,37] consider a 3-D non-Gaussian field over an area A for a time period of D. Clearly, the area cannot be too large since the wave field may not be homogeneous. The duration should be short so that spectral changes occurring in time are not so significant and the sea state can be assumed as stationary. Then, the third-order nonlinear probability $P^{(nl)}_{\rm FST}(\xi; A, D)$ that the maximum surface elevation $\eta_{\max}$ over the area A and during the time interval D exceeds the generic threshold ξH_s is equal to the probability of exceeding the threshold ξ_0, which accounts for kurtosis effects only, that is

$$P^{(nl)}_{\rm FST}(\xi; A, D) = P_{\rm ST}(\xi_0; A, D)\left(1 + \Lambda\xi_0^2(4\xi_0^2 - 1)\right). \tag{9}$$

The Gaussian probability of exceedance

$$P_{\rm ST}(\xi; A, D) = \Pr\{\eta_{\max} > \xi H_s\} = (16M_3\xi^2 + 4M_2\xi + M_1)P_{\rm R}(\xi), \tag{10}$$

where $P_{\rm R}(\xi)$ is the Rayleigh exceedance probability of Eq. (14).

Here, M_1 and M_2 are the average number of 1-D and 2-D waves that can occur on the edges and boundaries of the volume Ω, and M_3 is the average number of 3-D waves that can occur within the volume.[32] These all depend on the directional wave spectrum and its spectral moments m_{ijk} and are given in Appendix A.2.

The amplitude ξ accounts for both skewness and kurtosis effects and it relates to ξ_0 via the Tayfun (1980) quadratic equation

$$\xi = \xi_0 + 2\mu\xi_0^2. \tag{11}$$

Further, the statistical parameters μ and Λ are defined in section 3.

Given the probability structure of the wave surface defined by Eq. (9), the nonlinear mean maximum surface or crest height $\overline{h}_{\rm FST} = \xi_{\rm FST}H_s$ attained over the area A during a time interval D is given, according to Gumbel (1958), by

$$\xi_{\rm FST} = \overline{h}_{\rm FST}/H_s = \xi_{\rm m} + 2\mu\xi_{\rm m}^2 + \frac{\gamma_e\,(1 + 4\mu\xi_{\rm m})}{16\xi_{\rm m} - \frac{32M_3\xi_{\rm m}+4M_2}{16M_3\xi_{\rm m}^2+4M_2\xi_{\rm m}+M_1} - \Lambda G(\xi_{\rm m})}, \tag{12}$$

where the most probable surface elevation value $\xi_{\rm m}$ satisfies $P_{\rm FST}(\xi_{\rm m}; A, D) = 1$, or equivalently from Eq. (9)

$$(16M_3\xi_{\rm m}^2 + 4M_2\xi_{\rm m} + M_1)P_{\rm R}(\xi_{\rm m})\left(1 + \Lambda\xi_{\rm m}^2(4\xi_{\rm m}^2 - 1)\right) = 1,$$

and

$$G(\xi_{\rm m}) = \frac{2\xi_{\rm m}(8\xi_{\rm m}^2 - 1)}{1 + \Lambda\xi_{\rm m}^2(4\xi_m^2 - 1)}.$$

The nonlinear mean maximum surface or crest height $h_{\rm T}$ expected at a point during the time interval D follows from Eq. (12) by setting $M_2 = M_3 = 0$ and $M_1 = N_{\rm D}$, where $N_{\rm D} = D/\bar{T}$ denotes the number of wave occurring during D and $\bar{T}$ is the mean up-crossing period (see Appendix A.2). The linear mean counterpart follows from Eq. (12) by setting $\mu = 0$ and $\Lambda = 0$.

The statistical interpretations of the probability $P_{\rm FST}^{(nl)}(\xi; A, D)$ and associated space-time average maximum $\overline{h}_{\rm FST}$ are as follows. Consider an ensemble of N realizations of a stationary and homogeneous sea state of duration D, each of which has similar statistical structure to the El Faro wave field. On this basis, there would be N samples, say $(\eta_{\rm max}^{(1)}, ..., \eta_{\rm max}^{(N)})$ of the maximum surface height $\eta_{\rm max}$ observed within the area A during the time interval D. Then, all the maximum surface heights in the ensemble will exceed the threshold $\overline{h}_{\rm FST}$. Clearly, the maximum surface height can exceed by far such average. Indeed, only in a few number of realizations $N \cdot P_{\rm FST}^{(nl)}(\xi; A, D)$ out of the ensemble of N sea states, the maximum surface height exceeds a threshold $\xi H_s \gg \overline{h}_{\rm FST}$ much larger than the expected value.

To characterize such rare occurrences in third-order nonlinear random seas one can consider the threshold $h_q = \xi_q H_s$ exceeded with probability q by the maximum surface height $\eta_{\rm max}$ over an area A during a sea state of duration D. This satisfies

$$P_{\rm FST}^{(nl)}(\xi_q; A, D) = q. \tag{13}$$

The statistical interpretation of h_q is as follows: the maximum surface height $\eta_{\rm max}$ observed within the area A during D exceeds the threshold h_q only in $q\,N$ realizations of the above mentioned ensemble of N sea states.

Note that for large areas, i.e. $\ell >> L_0$, the FST model as any other similar models available in literature[38–41] will overestimate the maximum surface height over an area and time interval because they all rely on Gaussianity. This implies that there are no physical limits on the values that the surface height can attain as the Gaussian model does not account for the saturation induced by the nonlinear dispersion[17] of ocean waves or wave breaking. Thus, the larger the area A or the time interval D, the greater the number of waves sampled in space-time, and unrealistically large waves are likely to be sampled in a Gaussian or weakly nonlinear Gaussian sea.

This point is elaborated further and demonstrated explicitly by way of the results displayed in Fig. (10). Here, the theoretical (FST) ratio $\overline{h}_{\rm FST}/\overline{h}_{\rm T}$ as a function of the area width ℓ/L_0 is shown for the El Faro, Draupner and Andrea sea states respectively. The FST ratios for Draupner and Andrea are estimated using the European Reanalysis (ERA)-interim data.[37] For comparisons, the empirical FST ratio from the El Faro HOS simulations together with the experimental observations at the Acqua Alta tower[33] are also shown. Recall that $\overline{h}_{\rm FST}$ is the mean maximum surface height expected over the area ℓ^2 during a sea state of duration $D = 1$ hour and $\overline{h}_{\rm T}$ is the mean maximum surface height expected at a point. Clearly, the theoretical FST ratio for El Faro fairly agrees with the HOS simulations for small areas ($\ell \leq L_0$), whereas it yields overestimation over larger areas. We argue that the saturation of the HOS FST ratio over larger areas is an effect of the nonlinear dispersion which is effective in limiting the wave growth as a precursor to breaking.[17,42]

Note that the FST ratios for all the three sea states are nearly the same for $\ell \leq L_0$. These results are very encouraging as they suggest possible statistical similarities and universal laws for space-time extremes in wind sea states. Moreover, for $\ell \sim L_0$ the mean wave surface maximum expected over the area is 1.35 times larger than that expected at a point in agreement with Acqua Alta sea observations.[33]

We point out that the FST model is suitable for offshore applications, where the interest is in the expected wave maxima over small areas such as those covered by oil platforms, i.e.

$\ell \leq L_0$. Thus, the space-time probability $P^{(nl)}_{\rm FST}(\xi; A, D)$ in Eq. (9) can be interpreted as the probability that the oil rig encounters a wave whose crest height is larger than the threshold ξH_s over the oil rig footprint of area A and during a time span D.

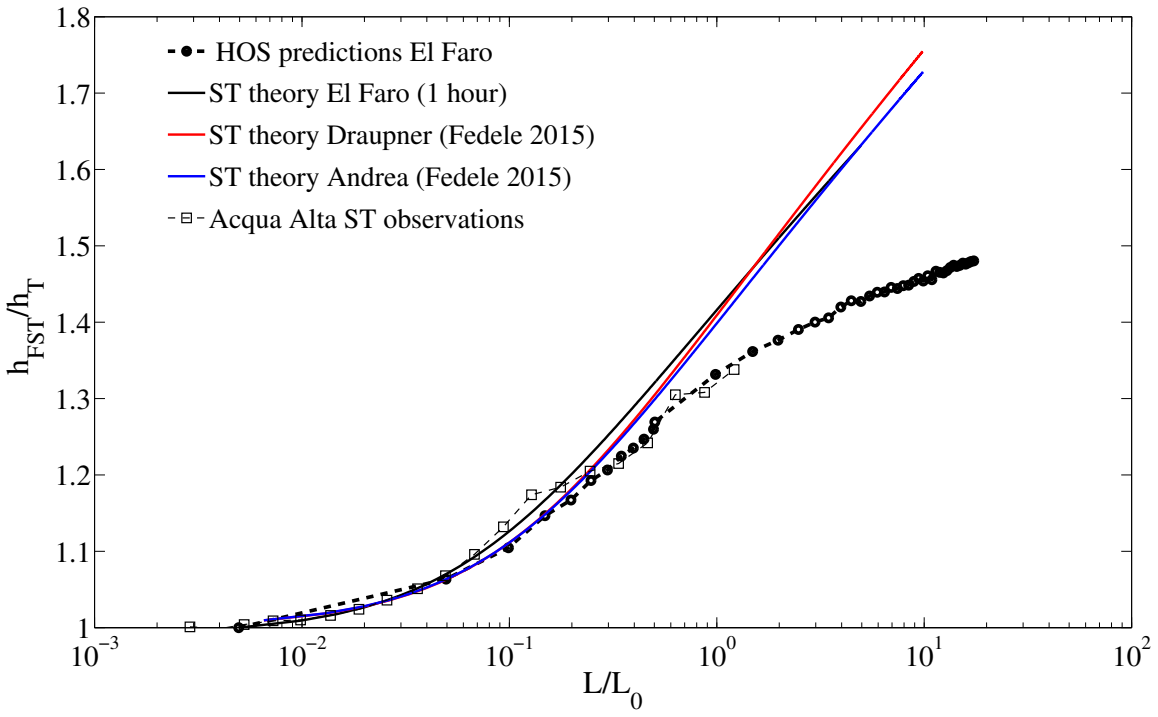

Figure 10: Space-time extremes: theoretical FST ratios $\overline{h}_{\rm FST}/\overline{h}_{\rm T}$ as a function of the area width ℓ/L_0 for El Faro (black), Draupner (red) and Andrea (blue) sea states, where $\overline{h}_{\rm FST}$ is the mean maximum surface height expected over the area ℓ^2 during a sea state of duration $D = 1$ hours and $\overline{h}_{\rm T}$ is the mean maximum surface height expected at a point. For comparisons, the empirical FST ratio from the El Faro HOS simulations (dashed line with circles) together with the experimental observations at the Acqua Alta tower (squares) are also shown.[33] L_0 is the mean wavelength.

7.2 The encounter probability of a rogue wave by the El Faro vessel

The data suggest that the El Faro vessel was drifting at an average speed of approximately 2.5 m/s prior to its sinking. This is considered in our analysis as follows. Define first the two events:

R= "El Faro encounters a rogue wave along its navigation route";

S= "El Faro sinks".

We know that the event S happened. Thus, one should consider the conditional probability

$$\Pr\{R|S\} = \frac{\Pr\{S\big|R\} \cdot \Pr\{R\}}{\Pr\{S\}}. \tag{14}$$

Here, $\Pr\{S\}$ is the unconditional probability of the event that El Faro sinks. This could be estimated from worldwide statistics of sunk vessels with characteristics similar to El Faro. $\Pr\{S|R\}$ is the conditional probability that El Faro sinks given that the vessel encountered a rogue wave. This probability can be estimated by Monte Carlo simulations of the nonlinear interaction of the vessel with the rogue wave field.

Our rogue wave analysis provides an estimate of the unconditional probability $\Pr\{R\}$ that El Faro encounters a rogue wave along its navigation or drifting route by means of the encounter probability $P_e(h)$. This is the probability that a vessel along its navigation path encounters a rogue wave whose crest height exceeds a given threshold h. Clearly, the probability P_e that El Faro encounters a rogue wave while drifting is higher than that if the vessel would be anchored at a fixed location like an oil platform.[32] Indeed, the encounter of a rogue wave by a moving vessel is analogous to that of a big wave that a surfer is in search of. His likelihood to encounter a big wave increases if he moves around a large area instead of staying still. If the surfer spans a large area the chances to encounter a large wave increase. This is a space-time effect which is very important for ship navigation and must be accounted for.[32,43–45]

In this section, the encounter probability $P_e(h)$ is formulated as follows. Consider a random wave field whose surface elevation at a given point (x, y) in a fixed frame at time t is $\eta(x, y, t)$. Consider a vessel of area A that navigates through the wave field at a constant speed V along a straight path at an angle β with respect to the x axis. Define also (x_e, y_e) as a cartesian frame moving with the ship. Then, the line trajectories of any point (x_e, y_e) of the vessel in the fixed frame are given by

$$x = x_e + V\cos(\beta)t, \quad y = x_e + V\sin(\beta)t, \tag{15}$$

where for simplicity we assume that at time $t = 0$ the center of gravity of the vessel is at the origin of the fixed frame.

The surface height $\eta_c(t)$ encountered by the moving vessel, or equivalently the surface fluctuations measured by a wave probe installed on the ship, is

$$\eta_c(x_e, y_e, t) = \eta(x_e + V\cos(\beta)t, y_e + V\cos(\beta)t, t), \tag{16}$$

If η is a Gaussian wave field homogeneous in space and stationary in time, then so is η_c with respect to the moving frame (x_e, y_e, t). The associated space-time covariance is given by

$$\Psi(X, Y, T) = \overline{\eta_c(x_e, y_e, t)\eta_c(x_e + X, y_e + Y, t + T)} = \int S(f, \theta)\cos(k_x X + k_y Y - 2\pi f_e T)\mathrm{d}f\mathrm{d}\theta, \tag{17}$$

where $k_x = k\cos(\theta)$, $k_y = k\sin(\theta)$ and k is the wavenumber associated with the frequency f by way of the wave dispersion relation. As a result of the Doppler effect, the encountered, or apparent frequency is[43–45]

$$f_e = f - kV\cos(\theta - \beta)/(2\pi), \tag{18}$$

and $S(f, \theta)$ is the directional wave spectrum of the sea state. Note that when the vessel moves faster than waves coming from a direction θ, the apparent frequency $f_e < 0$ and for

an observer on the ship waves appear to move away from him/her. In this case, the direction of those waves should be reversed,[43] i.e. $\theta = \theta + \pi$, and f_e set as positive.

The spectral moments $m^{(e)}_{ijk}$ of the encountered random field readily follow from the coefficients of the Taylor series expansion of $\Psi(X, Y, T)$ around $(X = 0, Y = 0, T = 0)$. In particular,

$$m^{(e)}_{ijk} = \frac{\partial^{i+j+k}\Psi}{\partial X^i \partial Y^j \partial T^k}\Big|_{X=Y=T=0} = \int S(f,\theta) k_x^i k_y^j f_e^k \mathrm{d}f\mathrm{d}\theta. \tag{19}$$

The nonlinear space-time statistics can then easily processed by using the encountered spectral moments $m^{(e)}_{ijk}$ as described in section 7.1. Note that for generic navigation routes the encountered wave field η_c is a non-stationary random process of time. Thus, the associated spectral moments are time-varying. The space-time statistics can be still computed by first approximating the navigation route by a polygonal line made of piecewise straight segments along which the random process η_c is assumed as stationary.

Fig. (11) illustrates the HOS and theoretical predictions for the normalized nonlinear threshold h_n/H_s exceeded with probability $1/n$. In particular, a fixed observer at a point of the ocean has a probability $P_e \sim 10^{-6}$ to encounter a wave whose crest height exceeds the threshold $1.6H_s \approx 14$ m (red lines). On the contrary, the same probability increases to $3 \cdot 10^{-4}$ if the observer moves along the straight path Γ spanned by El Faro drifting against the dominant wave direction over a time interval of 10 minutes (blue lines). If we also account for the vessel size (241 x 30 m^2), the encounter probability P_e further increases to 1/400 (black lines).

Finally, we observed that the encounter probability does not scale linearly with time because of nonlinearities that reduce the natural dispersion of waves. Indeed, assuming that El Faro drifts over a time interval 5 times longer (50 minutes), the encounter probability just increases roughly by 3 times, $\sim 1/130$.

8 Breaking onset of the simulated rogue waves

Breaking waves remain a centrally-important unresolved phenomenon at the wind-driven sea surface. Despite the abundant literature and theories on rogue wave formation, the physical understanding and relation to wave breaking are still open problems. To date it is still unclear why breaking waves occur much more frequently than large or rogue waves. There remain fundamental knowledge gaps on the physical mechanisms that lead to breaking. Indeed, since breaking waves are statistically neither taller nor steeper than the significant waves,[46] if rogue waves do break what are the physical mechanisms that lead the wave to break and inhibit wave growth?

It has been well-known for decades that the dominant open ocean waves evolve in unsteady groups, with strong local variations in wave height within the groups. Group structure is a generic feature of such dispersive wave systems, in which different wave scales propagate with different speeds and exhibit complex behaviour, especially in focal zones where rapid wave energy convergence leads to very steep waves and conditions especially conducive for wave breaking. Extreme waves within groups play a central role in wave-driven circulation through Stokes drift and in upper-ocean mixing, through wave breaking and Langmuir

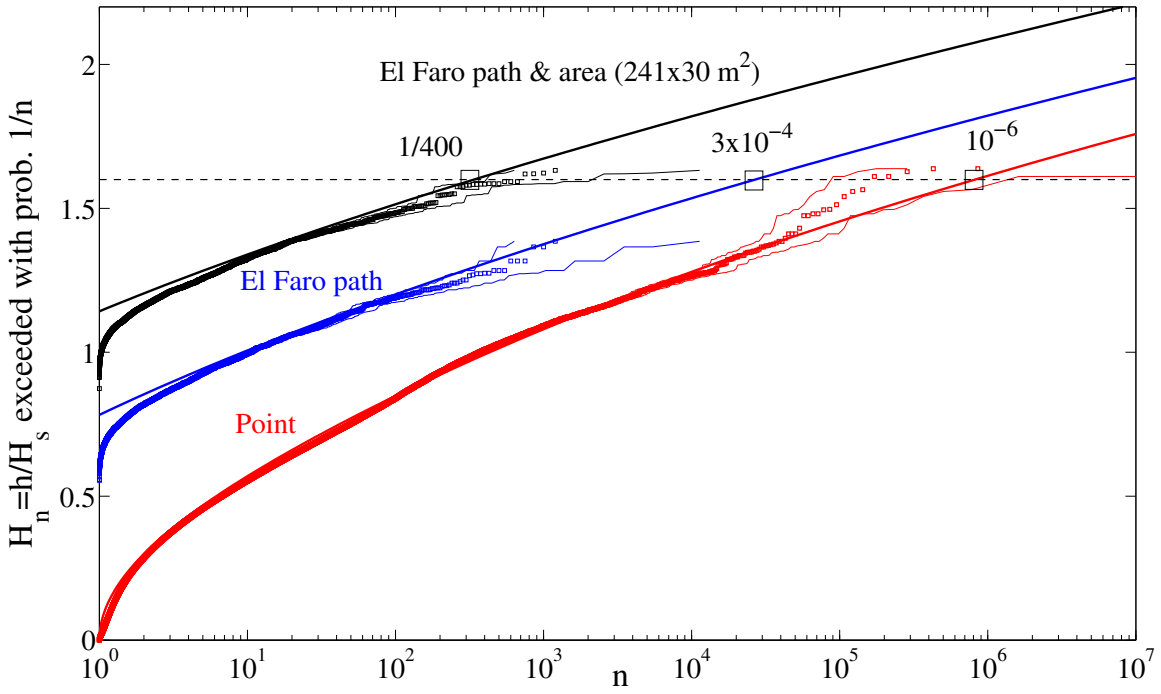

Figure 11: HOS (squares) and theoretical (solid lines) predictions for the normalized nonlinear threshold h_n/H_s exceeded with probability $1/n$ i) along the straight path Γ spanned by El Faro while drifting against the dominant wave direction at an estimated approximate average speed of 2.5 m/s over a time interval of 10 minutes (blue), ii) and also accounting for the vessel size (241 x 30 m^2) (black), and at a point and given time (red). Confidence bands are also shown (light dashes). The horizontal line denotes the threshold $1.6H_s \approx 14$ m, which is exceeded with probability 1/400, $3 \cdot 10^{-4}$ and 10^{-6} for the three cases shown.

turbulence. However, knowledge of the space-time structure of these wave groups remains fragmentary, and there exist many fundamental knowledge gaps, especially in regard to breaking waves.

Recently an elusive knowledge gap associated with ocean wave groups has been reconciled. In particular, several studies over the past two decades have suggested that the initial speeds of breaking crests of dominant waves within groups are typically 20% lower than the expected speed from linear wave theory (e.g.,[47] amongst others). This paradoxical contrast between long-held theory and observations has been resolved by.[17,48,49] Here, the crest slowdown is identified as a fundamental property of ocean waves as they naturally occur within evolving groups. Approaching the maximum of the group, each wave crest tilts forward, relaxes to symmetry at its tallest state, then the crest tilts backwards. As it approaches its maximum height, the wave crest decelerates significantly, typically by 20%, and either breaking begins or the height of the non-breaking wave decreases. Banner et al.[48] validated these findings for ocean waves from novel sea tower observations using the state-of-the-art Wave Acquisition Stereo System (WASS).[33] Clearly, the crest slowdown is a generic behaviour that precedes breaking within unsteady wave groups, and it also adds important new insights into the

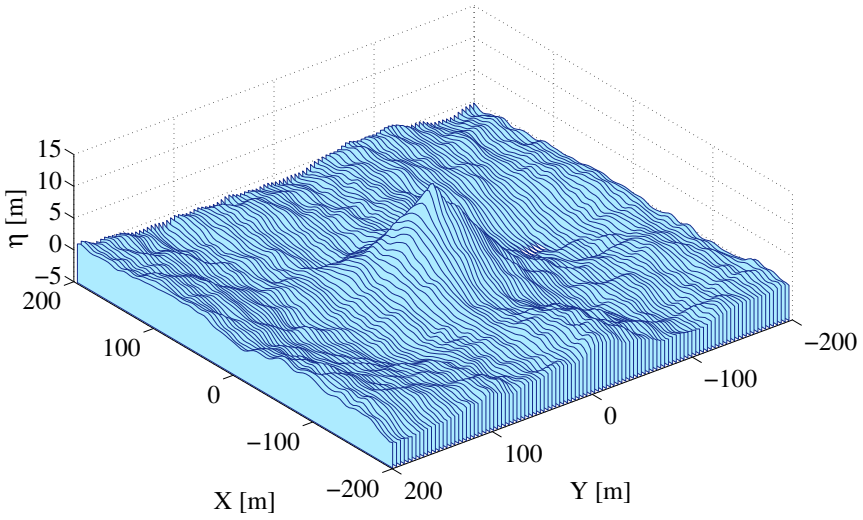

Figure 12: Expected spatial shape of a rogue wave whose crest height is $> 1.6H_s \approx 14$ m.

physical mechanisms that underpin rogue wave formation.

In this regard, recent theoretical analysis of the properties of water wave groups indicates possible physical mechanisms conducive to breaking.[17] These studies suggest that nonlinear wave dispersion may be the leading cause of the observed change in behavior of the wave dynamics from crest growth to breaking as the wave amplitude progressively increases. This change is associated with an increase in the growth of kinetic energy with respect to potential energy. An hypothesis for the breaking of rogue waves is that potential energy growth is inhibited: nonlinear dispersion limits the crest slowdown of deep-water ocean waves leading to breaking in a form of superharmonic instability.[17,42]

Moreover, recent studies show that the breaking onset of the largest crest of unsteady wave groups initiates before the horizontal particle velocity U_x reaches the crest speed V_c, with x being the direction of wave propagation. More specifically, it has been observed that wave breaking initiates when the particle velocity reaches approximately 0.84 times the crest velocity.[50–52] In fact, none of the recurrent groups reach the threshold $B_x = U_x/V_c D < 0.84$, while all marginal breaking cases exceed the threshold. Here, the physics of breaking onset can be linked to excess energy fluxes associated with the underlying unsteady wave group structure, where intra-group energy flux locally exceeds a stability level at the tallest crest, causing this crest to break. Indeed, it is found that B_x is also the wave energy flux $F_x = EU_x$ at the surface crest normalized by EV_c, where $E = \rho g\eta + K_e$ is the total wave energy at the crest, η the surface height and K_e the associated kinetic energy.[52] In this regard, recent studies[53] explored the existence of an energy flux threshold related to the breaking onset. This suggests looking at the space–time transport of wave energy fluxes near a large crest of an unsteady wave group and possible local superharmonic instabilities that initiate as the threshold B_x is exceeded leading to breaking, as those found for steady steep waves.[54] Thus, both the particle kinematics on the free surface and the energetics of the wave field that generates the surface should be considered to establish if the kinematic criterion for

incipient breaking is valid.

Our HOS simulations indicate that the simulated rogue waves of the El Faro sea state are nearly close to the breaking onset as the ratio B_x increases and tends to saturate at about 0.8 as the rogue wave amplitude increases. The saturation is mainly due to the nonlinear dispersion and it is an energy limiter for rogue waves. Note that our HOS simulations do not account for any dissipation mechanism due to breaking.

9 Conclusions

Our statistical analysis of the 1-hour sea state of Hurricane Joaquin during which the El Faro vessel sank indicates that a fixed observer at a given point of the ocean encounters a rogue wave whose crest height from the mean sea level exceeds 14 meters ($\sim 1.6H_s$) with a very small probability $P_e \sim 10^{-6}$, where H_s is the significant wave height of the sea state defined as four times the standard deviation of surface wave elevations. This probability estimate is of the same order as those for the Andrea and Draupner rogue waves, observed at different oil platforms in the North Sea in 1995 and 2007, respectively and the Killard rogue wave observed off the coast of Ireland in 2015.[2]

Data suggest that the El Faro vessel was drifting at an average speed of approximately 2.5 m/s prior to its sinking. Thus, consider an observer that moves along the straight path Γ spanned by El Faro drifting over a time interval of 10 minutes. Our analysis indicate that the moving observer has a higher probability to encounter a wave whose crest height exceeds the threshold $1.6H_s$, i.e. $P_e \sim 3 \cdot 10^{-4}$. If we also account for the vessel size (241 x 30 m^2), the encounter probability P_e is higher and close to 1/400. We also observe that P_e does not scale linearly with time because of nonlinearities that reduce the natural dispersion of waves. For example, P_e just increases roughly by 3 times to $\sim$ 1/130 if the vessel drifts over a time interval 5 times longer (50 minutes).

We point out that the encounter probability P_e is unconditional as it is not conditioned on the event that the sinking of El Faro happened.

The predicted rogue wave for El Faro has similar generating mechanism and characteristics of the Andrea, Draupner and Killard rogue waves as the constructive interference of elementary waves enhanced by bound nonlinearities and space-time effects, in agreement with recent studies.[2,32]

An analysis of the kinematics of the simulated rogue waves indicate that such waves were nearly incipient breaking, suggesting that larger rogue events are less likely to occur.[17,42]

10 Recommendations

The impact of our studies is two-fold. On the one hand, the present statistical analysis provides the basis for an improved understanding of how rogue waves originate during hurricanes. On the other hand, the proposed stochastic model for the encounter probability of a rogue wave provides the basis in the next generation of wave forecast models for a predictive capability of wave extremes and early warnings for shipping companies and others to avoid

dangerous areas at risk of rogue waves. However, further studies and analysis are needed. In particular, we recommend:

1. to perform HOS simulations of the El Faro sea state over larger areas $\geq 16km^2$ to further validate and improve the statistics and prediction of rogue waves presented in this report.

2. the proposed formulation of the encounter probability P_e is unconditional as it is not conditioned on the event that the sinking of El Faro happened. Thus, we suggest to estimate the conditional probability $\Pr\{R|S\}$ in Eq. (14) that El Faro encountered a rogue wave given that the sinking of the vessel occurred. This requires Monte Carlo simulations of the nonlinear interaction of the vessel with a rogue wave field;

3. to perform HOS simulations of the El Faro sea state accounting for both wind input and wave breaking and study their effects on the statistics and prediction of rogue waves;

4. further studies on the breaking onset of the simulated rogue waves, which will allow to quantify the maximal crest amplitudes attainable during intense hurricane-generated sea states and improvements of probabilistic models, which to date do not account for nonlinear wave dispersion and breaking.

5. the theoretical predictions of space-time extremes based on the proposed Gaussian-based FST model fairly agree with the HOS simulations for small areas with width $\ell \leq L_0$, where L_0 is the mean wavelength. On the contrary, the FST model overestimates the maximum surface height over larger areas ($\ell > L_0$) and so any other similar models.[38–41] This is because in a Gaussian or weakly nonlinear Gaussian sea unrealistically large waves are likely to be sampled over large areas or long time intervals. We argue that in realistic oceanic seas nonlinear wave dispersion is effective in limiting the wave growth as a precursor to breaking.[17] Studies by the first author are in progress to improve the proposed probabilistic model for the encounter probability of a rogue wave accounting for both nonlinear wave dispersion and breaking.

Appendix A Methods

A.1 Wave parameters

The significant wave height H_s is defined as the mean value $H_{1/3}$ of the highest one-third of wave heights. It can be estimated either from a zero-crossing analysis or more easily from the wave omnidirectional spectrum $S_o(f) = \int_0^{2\pi} S(f,\theta)\mathrm{d}\theta$ as $H_s \approx 4\sigma$, where $\sigma = \sqrt{m_0}$ is the standard deviation of surface elevations, $m_j = \int S_o(f) f^j \mathrm{d}f$ are spectral moments. Further, $S(f,\theta)$ is the directional wave spectrum with θ as the direction of waves at frequency f, and the cyclic frequency is $\omega = 2\pi f$.

The dominant wave period $T_p = 2\pi/\omega_p$ refers to the cyclic frequency ω_p of the spectral peak. The mean zero-crossing wave period T_0 is equal to $2\pi/\omega_0$, with $\omega_0 = \sqrt{m_2/m_0}$.

The associated wavelength $L_0 = 2\pi/k_0$ follows from the linear dispersion relation $\omega_0 = \sqrt{gk_0 \tanh(k_0 d)}$, with d the water depth. The mean spectral frequency is defined as $\omega_m = m_1/m_0$[9] and the associated mean period T_m is equal to $2\pi/\omega_m$. A characteristic wave steepness is defined as $\mu_m = k_m\sigma$, where k_m is the wavenumber corresponding to the mean spectral frequency ω_m.[9] The following quantitites are also introduced: $q_m = k_m d, Q_m = \tanh q_m$, the phase velocity $c_m = \omega_m/k_m$, the group velocity $c_g = c_m\left[1 + 2q_m/\sinh(2q_m)\right]/2$. The spectral bandwidth $\nu = (m_0 m_2/m_1^2 - 1)^{1/2}$ gives a measure of the frequency spreading. The angular spreading $\sigma_\theta = \sqrt{\int_0^{2\pi} D(\theta)(\theta - \theta_m)^2 \mathrm{d}\theta}$, where $D(\theta) = \int_0^\infty S(\omega,\theta)\mathrm{d}\omega/\sigma^2$ and $\theta_m = \int_0^{2\pi} D(\theta)\theta \mathrm{d}\theta$ is the mean direction. Note that $\omega_0 = \omega_m\sqrt{1+\nu^2}$.

The parameter $\Lambda = \lambda_{40} + 2\lambda_{22} + \lambda_{04}$ is a measure of third-order nonlinearities and is a function of the fourth order cumulants λ_{nm} of the wave surface η and its Hilbert transform $\hat{\eta}$.[10] In particular, $\lambda_{22} = \overline{\eta^2\hat{\eta}^2}/\sigma^4 - 1$ and $\lambda_{04} = \overline{\hat{\eta}^4}/\sigma^4 - 3$. In practice, Λ is usually approximated solely in terms of the excess kurtosis as $\Lambda_{\mathrm{appr}} = 8\lambda_{40}/3$ by assuming the relations between cumulants[55] $\lambda_{22} = \lambda_{40}/3$ and $\lambda_{04} = \lambda_{40}$. These, to date, have been proven to hold for linear and second-order narrowband waves only.[11] For third-order nonlinear seas, our numerical studies indicate that $\Lambda \approx \Lambda_{\mathrm{appr}}$ within a 3% relative error in agreement with observations.[56,57] The Tayfun wave steepness $\mu = \lambda_3/3$ relates to the wave skewness λ_3 of surface elevations.

A.2 Space-Time Statistical Parameters

For space-time extremes, the coefficients in Eq. (10) are given by[32,58]

$$M_3 = 2\pi \frac{D}{\overline{T}} \frac{\ell_x}{\overline{L_x}} \frac{\ell_y}{\overline{L_y}} \alpha_{xyt},$$

$$M_2 = \sqrt{2\pi}\left(\frac{D}{\overline{T}}\frac{\ell_x}{\overline{L_x}}\sqrt{1-\alpha_{xt}^2} + \frac{D}{\overline{T}}\frac{\ell_y}{\overline{L_y}}\sqrt{1-\alpha_{yt}^2} + \frac{\ell_x}{\overline{L_x}}\frac{\ell_y}{\overline{L_y}}\sqrt{1-\alpha_{xy}^2}\right),$$

$$M_1 = N_D + N_x + N_y,$$

where

$$N_D = \frac{D}{\overline{T}}, \qquad N_x = \frac{\ell_x}{\overline{L_x}}, \qquad N_y = \frac{\ell_y}{\overline{L_y}}$$

are the average number of waves occurring during the time interval D and along the x and y sides of length ℓ_x and ℓ_y respectively. They all depend on the mean period $\overline{T}$, mean wavelengths $\overline{L_x}$ and $\overline{L_y}$ in x and y directions:

$$\overline{T} = 2\pi\sqrt{\frac{m_{000}}{m_{002}}}, \qquad \overline{L_x} = 2\pi\sqrt{\frac{m_{000}}{m_{200}}}, \qquad \overline{L_y} = 2\pi\sqrt{\frac{m_{000}}{m_{020}}}$$

and

$$\alpha_{xyt} = \sqrt{1 - \alpha_{xt}^2 - \alpha_{yt}^2 - \alpha_{xy}^2 + 2\alpha_{xt}\alpha_{yt}\alpha_{xy}}.$$

Here,

$$m_{ijk} = \iint k_x^i k_y^j f^k S(f,\theta) df d\theta$$

are the moments of the directional spectrum $S(f,\theta)$ and

$$\alpha_{xt} = \frac{m_{101}}{\sqrt{m_{200}m_{002}}}, \qquad \alpha_{yt} = \frac{m_{011}}{\sqrt{m_{020}m_{002}}}, \qquad \alpha_{xy} = \frac{m_{110}}{\sqrt{m_{200}m_{020}}}.$$

A.3 The Higher Order Spectral (HOS) numerical method

The Mixed Eulerian Lagrangian (MEL) and the High-Order Spectral (HOS) methods are two reliable numerical schemes for solving the the time evolution of the wave motion of an inviscid and irrotational fluid with a surface.

MEL splits the kinematic problem (Eulerian step), which solves the spatial distribution of the kinematic field, from the dynamic problem (Lagrangian step), which solves the temporal evolution of the kinematic quantities at the free-surface.[59] In particular, the Eulerian step is a linear Cauchy problem for the wave potential, which is usually reformulated as a boundary integral equation. The associated solution is determined at the surface by the Boundary Element Method. The Lagrangian step instead describes the evolution of the free surface through Lagrangian markers that can trace wave overturning of crests over troughs.

Conversely the HOS, developed independently by Dommermuth & Yue[23] and West *et al.*[24] is based on a perturbation expansion of the wave potential function up to a prescribed order M of nonlinearities in terms of a small parameter ε, a characteristic wave steepness. The HOS method solves for nonlinear wave-wave interactions (up to an arbitrary specified order M) of a large number $N = O(1000)$ of free waves (i.e. Fourier modes) on the undisturbed free-surface plane. A pseudo-spectral technique is used to solve for the associated Boundary Value Problem (BVP). This ensures a computational cost which scales linearly with N and M, guaranteeing high computational efficiency for large spatial domains.

Hereafter, we will briefly describe the theoretical formulation of the HOS solver. Let $\vec{r} \equiv (x,y,z)$ be a Cartesian coordinate system with $\vec{x} \equiv (x,y)$ coincident with the mean water level and the z axis upwards. The ideal flow assumption enables the definition of a velocity potential function $\Phi(\vec{x},z,t)$, whose gradient determines the fluid velocity on the whole field V. To impose mass conservation, Φ satisfies the Laplace equation within the fluid domain

$$\nabla^2\Phi = 0 \quad in \quad V$$

and boundary conditions at the free surface, lateral boundaries and sea bottom.

Then, a velocity potential can defined on the free surface $z = \eta(x,t)$ as,[?]

$$\Phi^s(\vec{x},t) \equiv \Phi(\vec{x},\eta(\vec{x},t),t) \tag{20}$$

and it is assumed as continuous and single-valued. The free-surface boundary conditions are then written in terms of the potential Φ^s as:

$$\eta_t + \vec{\nabla}_{\vec{x}}\eta \cdot \vec{\nabla}_{\vec{x}}\Phi^s - \left(1 + \vec{\nabla}_{\vec{x}}\eta \cdot \vec{\nabla}_{\vec{x}}\eta\right)\Phi_z(\vec{x},\eta,t) = 0 \tag{21}$$

$$\Phi^s_t + g\eta + \frac{1}{2}\vec{\nabla}_{\vec{x}}\Phi^s \cdot \vec{\nabla}_{\vec{x}}\Phi^s - \frac{1}{2}\left(1 + \vec{\nabla}_{\vec{x}}\eta \cdot \vec{\nabla}_{\vec{x}}\eta\right)\Phi^2_z(\vec{x},\eta,t) = -\frac{P_F}{\rho} \tag{22}$$

From the above equations, the solution of the free-surface wave field at each time step requires solving for a Dirichlet BVP of the Lapace equation for the potential Φ on the instantaneous free-surface wave elevation $\eta(\vec{x},t)$, in order to get the vertical velocity Φ_z.

A peculiar feature of the HOS formulation is the efficient strategy proposed for the solution of the Dirichlet BVP. This is based on a direct use of perturbation expansion in the small parameter $\varepsilon = ka$, the wave steepness, with k the wave number and a the wave amplitude. At a given time t, the velocity potential is written as a perturbation series in ε up to a prescribed order M

$$\Phi\left(\vec{x},z,t\right) = \sum_{m=1}^{M} \Phi^{(m)}\left(\vec{x},z,t\right) \tag{23}$$

where $\Phi^{(m)} = O\left(\varepsilon^m\right)$ are the perturbation potentials. A further expansion of each $\Phi^{(m)}$ in a Taylor series around the mean free surface $z = 0$ yields

$$\Phi^s\left(\vec{x},t\right) = \Phi\left(\vec{x},\eta,t\right) = \sum_{m=1}^{M}\sum_{\ell=0}^{M-m} \frac{\eta^\ell}{\ell!}\frac{\partial^\ell \Phi^{(m)}\left(\vec{x},0,t\right)}{\partial z^\ell} \tag{24}$$

Expanding (24) and regrouping terms at every order yield a sequence of Dirichlet boundary conditions for each unknown $\Phi^{(m)}$ on $z = 0$:

$$\Phi^{(m)}\left(\vec{x},0,t\right) = f^{(m)}, \qquad m = 1,2,\ldots,M \tag{25}$$

where

$$\begin{cases} f^{(1)} = \Phi^s \\ f^{(m)} = \sum\limits_{\ell=1}^{m-1} \frac{\eta^\ell}{\ell!}\frac{\partial^\ell \Phi^{(m-\ell)}}{\partial z^\ell}\Big|_{z=0}, \qquad m = 2,3,\ldots,M \end{cases}$$

Eq. (25) together with the Laplace equation satisfied by each potential $\Phi^{(m)}$ and associated boundary conditions define, at each given time t, a sequence of boundary value problems for $\Phi^{(m)} \quad m = 1,2,...,M$, in the domain $z <= 0$.

These are solved efficiently by way of a pseudo-spectral method. In particular, each $\Phi^{(m)}$ is represented through an eigenfunction expansion of free modes $\Psi_n\left(\vec{x},z\right)$:

$$\Phi^{(m)}\left(\vec{x},z,t\right) = \sum_{n=1}^{\infty} \Phi_n^{(m)}\left(t\right)\Psi_n\left(\vec{x},z\right), \qquad z \le 0$$

where $\Phi_n^{(m)}(t)$ is the amplitude of the n^{th} mode of the m^{th} perturbation potential. The mode functions are chosen to implicitly satisfy the Laplace equation along with its boundary conditions.

Dirichlet free-surface conditions enable the determination of the mode amplitudes in a recursive way through the use of the Fast Fourier Transform (FFT) algorithm. For numerical purpose, a finite number N of modes is considered, with N sufficiently large in order to capture the physical spatial scales of nonlinear wave-wave interactions.

Once the modal amplitudes $\Phi_n^{(m)}(t)$ have been determined at each time step, the vertical velocity on the free surface is computed as:

$$\Phi_z\left(\vec{x},\eta,t\right)=\sum_{m=1}^{M}\sum_{\ell=0}^{M-m}\frac{\eta^\ell}{\ell!}\sum_{n=1}^{N}\Phi_n^{(m)}\left(t\right)\left.\frac{\partial^{\ell+1}\Psi_n\left(\vec{x},z\right)}{\partial z^{\ell+1}}\right|_{z=0}$$

providing the final form of the free surface boundary conditions:

$$\eta_t+\vec{\nabla}_{\vec{x}}\eta\cdot\vec{\nabla}_{\vec{x}}\Phi^s-\left(1+\vec{\nabla}_{\vec{x}}\eta\cdot\vec{\nabla}_{\vec{x}}\eta\right)\left[\sum_{m=1}^{M}\sum_{\ell=0}^{M-m}\frac{\eta^\ell}{\ell!}\sum_{n=1}^{N}\Phi_n^{(m)}\left(t\right)\left.\frac{\partial^{\ell+1}\Psi_n\left(\vec{x},z\right)}{\partial z^{\ell+1}}\right|_{z=0}\right]=0 \quad (26)$$

$$\Phi_t^s+g\eta+\frac{1}{2}\vec{\nabla}_{\vec{x}}\Phi^s\cdot\vec{\nabla}_{\vec{x}}\Phi^s-\frac{1}{2}\left(1+\vec{\nabla}_{\vec{x}}\eta\cdot\vec{\nabla}_{\vec{x}}\eta\right)\left[\sum_{m=1}^{M}\sum_{\ell=0}^{M-m}\frac{\eta^\ell}{\ell!}\sum_{n=1}^{N}\Phi_n^{(m)}\left(t\right)\left.\frac{\partial^{\ell+1}\Psi_n\left(\vec{x},z\right)}{\partial z^{\ell+1}}\right|_{z=0}\right]^2=-\frac{P_F}{\rho} \quad (27)$$

which give the time evolution for Φ^s and η.

A suitable choice of the eigenfunctions enables the study of the wave propagation in different sea bottom conditions. The sea state is on deep waters, thus

$$\Psi_n(\vec{x},z)=e^{(|\vec{k}_n|z+i\vec{k}_n\cdot\vec{x})}$$

whit $\vec{k}_n=(k_{xn},k_{yn})$ the wave number vector. The associated discretized components in the wavenumber space are defined as:

$$\begin{cases} k_{xn}=\frac{2\pi n_x}{L_x} & n_x=0,\pm1,...,\pm(N_x-1) \\ k_{yn}=\frac{2\pi n_y}{L_y} & n_y=0,\pm1,...,\pm(N_y-1) \end{cases} \quad (28)$$

where N_x, N_y are the maximum numbers of Fourier modes along x and y, respectively, while L_x and L_y are the respective lengths of the physical domain.

Two different HOS formulations can be found in literature,[60] depending on the treatment of the last term in the LHS of the free-surface BC, i.e. eqs. (21)-(22), or equivalently, eqs. (26)-(27). By choosing for sake of simplicity the kinematic equation, [23] chooses the approximation

$$\left(1+\vec{\nabla}_{\vec{x}}\eta\cdot\vec{\nabla}_{\vec{x}}\eta\right)\Phi_z\left(\vec{x},\eta,t\right)\approx\left(\Phi_z\right)_M+|\vec{\nabla}_{\vec{x}}\eta|^2(\Phi_z)_M$$

with $(\Phi_z)_M=\sum_{m=1}^{M}\Phi_z^{(m)}$, while[24] uses

$$\left(1+\vec{\nabla}_{\vec{x}}\eta\cdot\vec{\nabla}_{\vec{x}}\eta\right)\Phi_z\left(\vec{x},\eta,t\right)\approx\left(\Phi_z\right)_M+|\vec{\nabla}_{\vec{x}}\eta|^2(\Phi_z)_{M-2}$$

A similar approximation can be used for the dynamic free-surface boundary conditions.

In our work, we will see the second HOS formulation,[24] which accounts for all the nonlinear terms at a given order of the perturbation expansion. Further, the HOS method relies on a pseudo-spectral solver and nonlinear terms are evaluated in physical space. This yield

unavoidable aliasing errors, which can be removed by a proper choice of the number of points P_x and Q_y in the physical space,[24] i.e.

$$\begin{cases} P_x \geq (M+1)N_x \\ Q_y \geq (M+1)N_y \end{cases} \tag{29}$$

Following West *et al.*,[24] time evolution of the free-surface wave field is done in the wavenumber space by way of a time integration of the single Fourier modes. To do so, a fourth-order Runge-Kutta method is used with a time step satisfying the CFL conditions

$$dt < \frac{dx}{min(C_x, C_y)}$$

with C_x and C_y indicating the significant phase speed along x and y, respectively, for the physical problem of interest.

The Potential Φ and wave surface elevation η are required at $t = 0$ as initial conditions for the simulations. Here, in order to simulate the sea state occurring around the time and region of the El Faro sinking, we used the hindcast directional spectrum estimated by WAVEWATCH III. In the wavenumber domain, the Fourier transform $\hat{\eta}(\mathbf{k})$ of η is constructed as $S(\mathbf{k})\exp(i\beta)$, where β is normally distributed over $[0, 2\pi]$. Similarly, the Fourier transform $\hat{\Phi}(\mathbf{k})$ of Φ is obtained via linear wave theory.

First, a sensitivity analysis on the discretization and the physical quantities influencing the statistics have been performed. Figure A13 shows the comparison of the omnidirectional wave spectrum $S_o(\omega)$ estimated from two simulations of the same third-order HOS algorithm on two different grids and for the same time of analysis (30 min). They have been obtained by halving both domain lengths L_x and L_y and keeping constant the number of Fourier modes along each direction. From Eqs. (28-29), this choice implies halving the spatial discretization of the simulated physical domain. The analysis confirms the substantial convergence of the HOS algorithm in terms of wave spectra, and the same trend is also observed for other statistical quantities, such as skewness and kurtosis.

We have also carried out a further analysis to test the performance of the HOS solver when the perturbation expansion for the wave potential Φ is retained up to third and fourth order, i.e. $M = 3$ and $M = 4$ respectively. In this regard, we ran distinct HOS simulations of the El Faro sea state for the two orders of the solver on the same grid and for the same temporal duration (30 min). We found that the associated omnidirectional wave spectra are practically indistinguishable as clearly seen in Figure A14. Thus, the wave dynamics is mostly governed by nonlinear interactions up to the third order, and second order bound nonlinearities are dominant in agreement with the recent analysis of rogue waves.[2] Thus, the HOS simulations of the El Faro sea state are carried out using a third-order scheme with $M = 3$.

We have also carried out simulations of the El Faro sea state using a third-order HOS scheme for two different sizes of the physical domain and sea state duration of 30 min. The grid spacing or spatial discretization is kept the same for both cases requiring doubling the number of Fourier modes for the larger domain in accordance with Eqs. (29) and (28). The predicted omnidirectional wave spectra $S_o(\omega)$ for the two simulated cases are very similar are

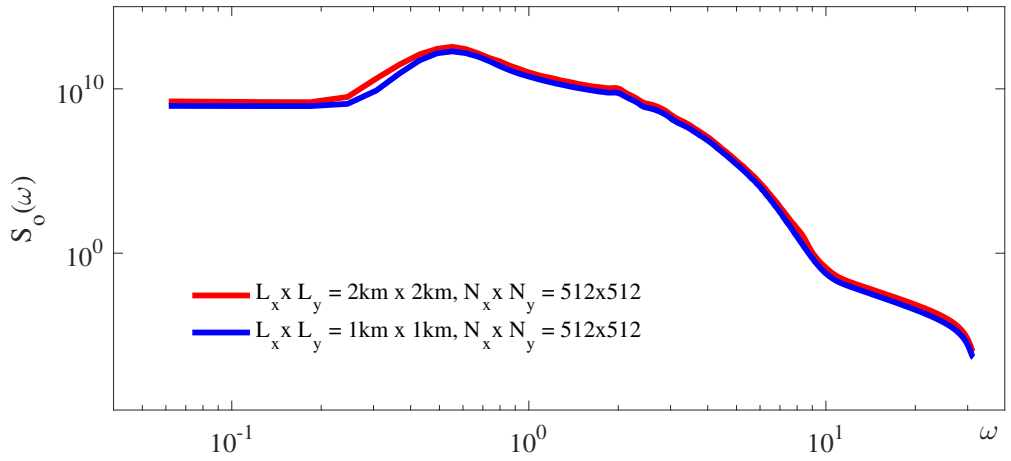

Figure A13: HOS simulations of the El Faro sea state: predicted omnidirectional wave spectra $S_o(\omega)$ as a function of the cyclic frequency ω using a third-order HOS scheme for two different spatial grids of a large spatial domain of size $L_x = L_y = 2000$ m (red curve) and an halved domain of size $L_x = L_y = 1000$ m (blue curve). Sea state duration 30 min and number of Fourier modes $N_x = N_y = 512$ for both cases.

clearly shown in Figure A15 as a further confirmation of the robust convergence properties of the HOS solver.

Finally, we have carried out HOS simulations of the El Faro sea state for different durations of 30 and 60 minutes respectively. The results indicate both the spectral and statistical properties of the sea state are practically the same for the two runs. Note that the HOS solver conserves mass and energy up to machine precision, even for a long simulation time of 60 min as illustrated in Figure A16.

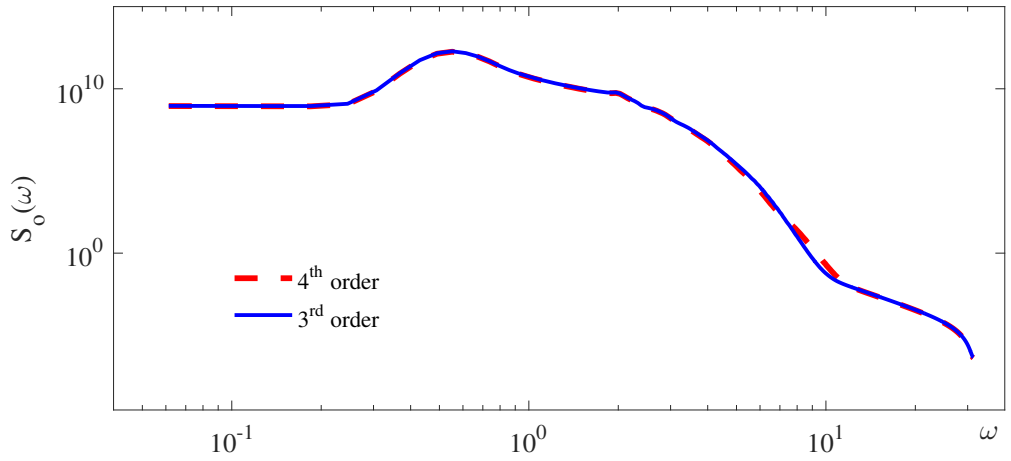

Figure A14: HOS simulations of the El Faro sea state: predicted omnidirectional wave spectra $S_o(\omega)$ as a function of the cyclic frequency ω using a third-order (continuous line) and a fourth-order (dashed line) HOS schemes (sea state duration 30 min). Same discretization is used for both cases, i.e. $L_x = L_y = 2000$ m and $N_x = N_y = 512$.

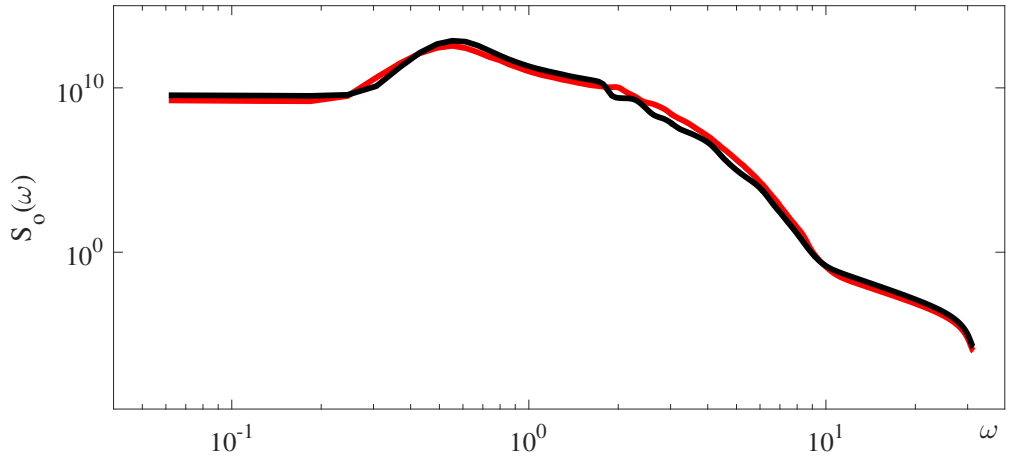

Figure A15: HOS simulations of the El Faro sea state: predicted omnidirectional wave spectra $S_o(\omega)$ as a function of the cyclic frequency ω using a third-order HOS scheme for two different sizes of the physical domain and sea state duration of 30 min Same discretization is used for both cases, i.e. $L_x = L_y = 2000$ m, $N_x = N_y = 512$ (red curve), and $L_x = L_y = 4000$ m, $N_x = N_y = 1024$ (black curve).

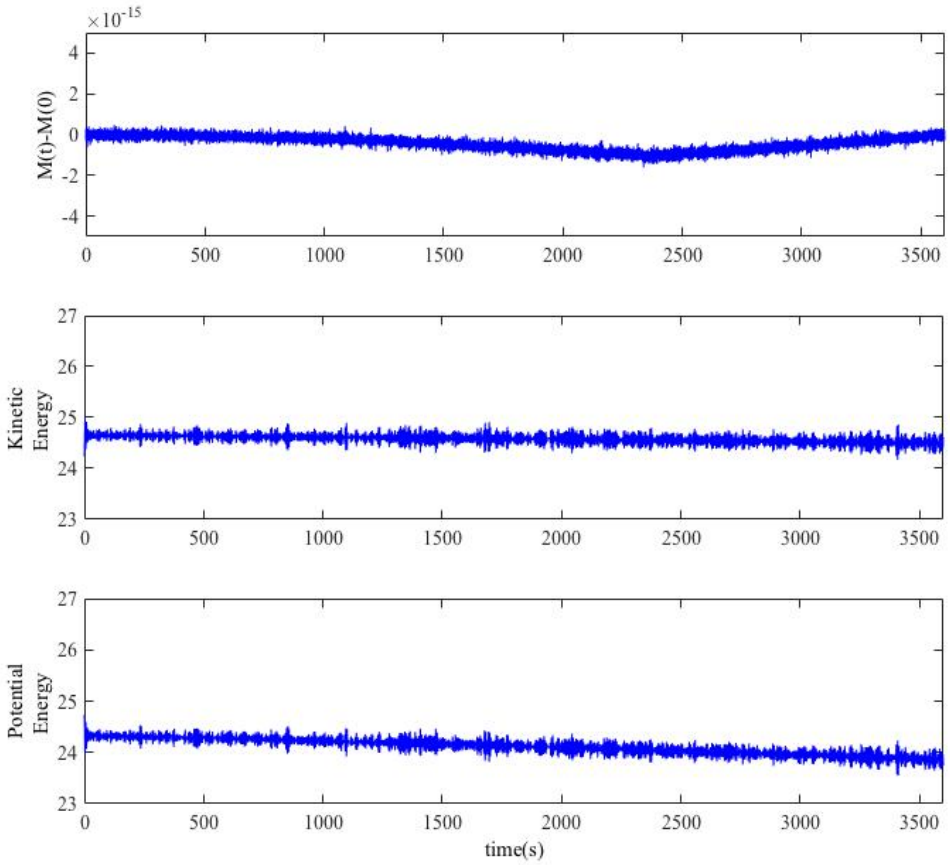

Figure A16: HOS simulations of the El Faro sea state: time evolution of the excess of mass (top), kinetic (center) and potential (bottom) energy. $L_x = L_y = 2000$ m, $N_x = N_y = 512$.

References

[1] HL Tolman and Development Group. User manual and system documentation of WAVEWATCH III version 4.18. Technical Report Tech. Note 316, NOAA/NWS/NCEP/MMAB, 2014.

[2] F. Fedele, J. Brennan, S. Ponce de León, J. Dudley, and F. Dias. Real world ocean rogue waves explained without the modulational instability. *Scientific Reports*, 6:27715 EP –, 06 2016.

[3] Peter A. E. M. Janssen and J. R. Bidlot. On the extension of the freak wave warning system and its verification. Tech. Memo 588, ECMWF, 2009.

[4] Peter A. E. M. Janssen. Nonlinear four-wave interactions and freak waves. *Journal of Physical Oceanography*, 33(4):863–884, 2003.

[5] M. A. Tayfun. Statistics of nonlinear wave crests and groups. *Ocean Engineering*, 33(11–12):1589 – 1622, 2006.

[6] F. Fedele. On the kurtosis of ocean waves in deep water. *Journal of Fluid Mechanics*, 782:25–36, 2015.

[7] P. A. E. M. Janssen. On some consequences of the canonical transformation in the hamiltonian theory of water waves. *Journal of Fluid Mechanics*, 637:1–44, 10 2009.

[8] F. Fedele and M. A. Tayfun. On nonlinear wave groups and crest statistics. *J. Fluid Mech*, 620:221–239, 2009.

[9] M. Aziz Tayfun. Narrow-band nonlinear sea waves. *Journal of Geophysical Research: Oceans*, 85(C3):1548–1552, 1980.

[10] M. Aziz Tayfun and Francesco Fedele. Wave-height distributions and nonlinear effects. *Ocean Engineering*, 34(11–12):1631 – 1649, 2007.

[11] M. A. Tayfun and J. Lo. Nonlinear effects on wave envelope and phase. *J. Waterway, Port, Coastal and Ocean Eng.*, 116:79–100, 1990.

[12] F. Fedele. Rogue waves in oceanic turbulence. *Physica D*, 237:2127–2131, 2008.

[13] Peter A. E. M. Janssen. On a random time series analysis valid for arbitrary spectral shape. *Journal of Fluid Mechanics*, 759:236–256, 11 2014.

[14] Nobuhito Mori, Miguel Onorato, and Peter A. E. M. Janssen. On the estimation of the kurtosis in directional sea states for freak wave forecasting. *Journal of Physical Oceanography*, 41(8):1484–1497, 2015/01/04 2011.

[15] M. Aziz Tayfun. Distributions of envelope and phase in wind waves. *Journal of Physical Oceanography*, 38(12):2784–2800, 2015/01/03 2008.

[16] Marios Christou and Kevin Ewans. Field measurements of rogue water waves. *Journal of Physical Oceanography*, 44(9):2317–2335, 2015/01/03 2014.

[17] Francesco Fedele. On certain properties of the compact zakharov equation. *Journal of Fluid Mechanics*, 748:692–711, 6 2014.

[18] M. Onorato, L. Cavaleri, S. Fouques, O. Gramstad, P.A.E.M. Janssen, J. Monbaliu, A. R. Osborne, C. Pakozdi, M. Serio, C. T. Stansberg, A. Toffoli, and K. Trulsen. Statistical properties of mechanically generated surface gravity waves: a laboratory experiment in a three-dimensional wave basin. *Journal of Fluid Mechanics*, 627:235–257, 5 2009.

[19] T. Waseda, T. Kinoshita, and H. Tamura. Evolution of a random directional wave and freak wave occurrence. *Journal of Physical Oceanography*, 39(3):621–639, 2015/04/05 2009.

[20] A. Toffoli, O. Gramstad, K. Trulsen, J. Monbaliu, E. Bitner-Gregersen, and M. Onorato. Evolution of weakly nonlinear random directional waves: laboratory experiments and numerical simulations. *Journal of Fluid Mechanics*, 664:313–336, 12 2010.

[21] S. Y. Annenkov and V. I. Shrira. Large-time evolution of statistical moments of wind–wave fields. *Journal of Fluid Mechanics*, 726:517–546, 7 2013.

[22] S. Y. Annenkov and V. I. Shrira. Evaluation of skewness and kurtosis of wind waves parameterized by JONSWAP spectra. *Journal of Physical Oceanography*, 44(6):1582–1594, 2014/12/21 2014.

[23] D. G. Dommermuth and D. K. P. Yue. A high-order spectral method for the study of nonlinear gravity waves. *Journal of Fluid Mechanics*, 184:267–288, 11 1987.

[24] B.J. West, K.A. Brueckner, R.S. Janda, M. Milder, and R.L. Milton. A new numerical method for surface hydrodynamics. *Journal of Geophysical Research*, 92:11803–11824, 1987.

[25] K. B. Dysthe, H. E. Krogstad, and P. Muller. Oceanic rogue waves. *Annual Review of Fluid Mechanics*, 40:287–310, 2008.

[26] K. Trulsen, J. C. Nieto Borge, O. Gramstad, L. Aouf, and J.-M. Lefèvre. Crossing sea state and rogue wave probability during the Prestige accident. *Journal of Geophysical Research: Oceans*, 120, 2015.

[27] J. Flanagan, E. Terry, E. Arabini, M. Djahanbani, B. Strong, J. Dudley, and F. Dias. ADCP measurements of extreme water waves off the west coast of Ireland. In *The Proceedings of the 26th (2016) International Offshore and Polar Engineering, Rhodes, Greece, June 26 - July 2, 2016*. International Society of Offshore and Polar Engineers, 2016.

[28] P. Boccotti. *Wave Mechanics for Ocean Engineering*. Elsevier Sciences, Oxford, 2000.

[29] D.A.G. Walker, P.H. Taylor, and R. Eatock Taylor. The shape of large surface waves on the open sea and the Draupner new year wave. *Applied Ocean Research*, 26(3–4):73 – 83, 2004.

[30] TAA Adcock, PH Taylor, S Yan, QW Ma, and PAEM Janssen. Did the Draupner wave occur in a crossing sea? *Proceedings of the Royal Society A: Mathematical, Physical and Engineering Science*, page rspa20110049, 2011.

[31] M. S. Longuet-Higgins and R. W. Stewart. Radiation stresses in water waves: a physical discussion, with applications. *Deep-Sea Research*, II:529 – 562, 1964.

[32] Francesco Fedele. Space–time extremes in short-crested storm seas. *Journal of Physical Oceanography*, 42(9):1601–1615, 2014/12/24 2012.

[33] Francesco Fedele, Alvise Benetazzo, Guillermo Gallego, Ping-Chang Shih, Anthony Yezzi, Francesco Barbariol, and Fabrice Ardhuin. Space–time measurements of oceanic sea states. *Ocean Modelling*, 70:103–115, 2013.

[34] Robert J Adler. *The geometry of random fields*, volume 62. Siam, 1981.

[35] Robert J Adler and Jonathan E Taylor. *Random fields and geometry*, volume 115. Springer Monographs in Mathematics, 2009.

[36] Robert J Adler. On excursion sets, tube formulas and maxima of random fields. *Annals of Applied Probability*, pages 1–74, 2000.

[37] F. Fedele. On oceanic rogue waves. *arXiv preprint arXiv:1501.03370*, 2015.

[38] Vladimir I Piterbarg. *Asymptotic methods in the theory of Gaussian processes and fields*, volume 148. AMS ser. Translations of Mathematical Monographs, 1995.

[39] H. Socquet-Juglard, K. B. Dysthe, K. Trulsen, H. E. Krogstad, and J. Liu. Probability distributions of surface gravity waves during spectral changes. *Journal of Fluid Mechanics*, 542:195–216, 11 2005.

[40] George Z Forristall. Maximum crest heights under a model tlp deck. In *ASME 2011 30th International Conference on Ocean, Offshore and Arctic Engineering*, pages 571–577. American Society of Mechanical Engineers, 2011.

[41] G. Z. Forristall. Maximum crest heights over an area: laboratory measurements compared to theory. In *ASME 2015 34th International Conference on Ocean, Offshore and Arctic Engineering*, number OMAE2015–41061. American Society of Mechanical Engineers, 2015.

[42] F. Fedele, C. Chandre, and M. Farazmand. Kinematics of fluid particles on the sea surface: Hamiltonian theory. *Journal of Fluid Mechanics*, 801:260–288, 2016.

[43] M. St. Denis and W. Pierson. On the motions of ships in confused seas. *Transactions, The Society of Naval Architects and Marine Engineers*, 61:280—357, 1953.

[44] G. Lindgren, I. Rychlik, and M. Prevosto. Stochastic doppler shift and encountered wave period distributions in gaussian waves. *Ocean Engineering*, 26(6):507 – 518, 1999.

[45] K. Podgórski, I. Rychlik, and U. E.B. Machado. Exact distributions for apparent waves in irregular seas. *Ocean Engineering*, 27(9):979–1016, 2000.

[46] L. H. Holthuijsen and T. H. C. Herbers. Statistics of breaking waves observed as whitecaps in the open sea. *AMS Journal of Physical Oceanography*, 16(2):290–297, 1986.

[47] R. J. Rapp and W. K. Melville. Laboratory measurements of deep-water breaking waves. *Philosophical Transactions of the Royal Society of London. Series A, Mathematical and Physical Sciences*, 331(1622):735–800, 1990.

[48] M. L. Banner, X. Barthelemy, F. Fedele, M. Allis, A. Benetazzo, F. Dias, and L. Peirson, W.˙ Linking reduced breaking crest speeds to unsteady nonlinear water wave group behavior. *Phys. Rev. Lett.*, 112:114502, Mar 2014.

[49] F. Fedele. Geometric phases of water waves. *EPL (Europhysics Letters)*, 107(6):69001, 2014.

[50] A. Saket, W.L. Peirson, M.L. Banner, X. Barthelemy, and M. Allis. Wave breaking onset of two–dimensional deep–water wave groups in the presence and absence of wind. *http://arxiv.org/abs/1508.07702*, 2015.

[51] X. Barthelemy, M.L. Banner, W.L. Peirson, F. Dias, , and M. Allis. On the local properties of highly nonlinear unsteady gravity water waves. part 1. slowdown, kinematics and energetics. *Journal of Fluid Mechanics (submitted) http://arxiv.org/abs/1508.06001*, 2015.

[52] X. Barthelemy, M.L. Banner, W.L. Peirson, F. Fedele, M. Allis, and F. Dias. On the local properties of highly nonlinear unsteady gravity water waves. part 2. dynamics and onset of breaking. *Journal of Fluid Mechanics (submitted) http://arxiv.org/abs/1508.06002*, 2015.

[53] Jin-Bao Song and Michael L. Banner. On determining the onset and strength of breaking for deep water waves. part i: Unforced irrotational wave groups. *Journal of Physical Oceanography*, 32(9):2541–2558, 2002.

[54] M. S. Longuet-Higgins and M. J. H. Fox. Theory of the almost-highest wave. Part 2. Matching and analytic extension. *Journal of Fluid Mechanics*, 85:769–786, April 1978.

[55] Nobuhito Mori and Peter A. E. M. Janssen. On kurtosis and occurrence probability of freak waves. *Journal of Physical Oceanography*, 36(7):1471–1483, 2013/08/11 2006.

[56] F. Fedele, Z. Cherneva, M. A. Tayfun, and C. Guedes Soares. Nonlinear Schrödinger invariants and wave statistics. *Physics of Fluids*, 22(3):036601, 2010.

[57] M. A. Tayfun and F. Fedele. Expected shape of extreme waves in storm seas. In *ASME 2007 26th International Conference on Offshore Mechanics and Arctic Engineering*, number OMAE2007–29073. American Society of Mechanical Engineers, 2007.

[58] A. Baxevani and I. Rychlik. Maxima for gaussian seas. *Ocean Engineering*, 33(7):895 – 911, 2006.

[59] M. S. Longuet-Higgins and E. D. Cokelet. The Deformation of Steep Surface Waves on Water. I. A Numerical Method of Computation. *Proc. R. Soc. A*, 350(1660):1–26, July 1976.

[60] M. Tanaka. A method of studying nonlinear random field of surface gravity waves by direct numerical simulation. *Fluid Dynamics Research*, 28:41–60, 2001.

Author contributions statement

The concept and design was provided by F. Fedele, who coordinated the scientific effort together with C. Lugni. C. Lugni and F. Fucile performed numerical simulations and developed specific codes for the analysis. The wave statistical analysis was performed by F. Fedele together with C. Lugni. The overall supervision was provided by F. Fedele; E. F. Campana made ongoing incisive intellectual contributions. All authors participated in the analysis and interpretation of results and the writing of the report.